Ex vivo recapitulation of intramuscular mRNA vaccination with naïve and recall antigens using a human Lymphoid Follicle Chip platform

Yunhao Zhai[1], Min Wen Ku[1], Ka Yang[2], Aditya Patil[1], Pranav Prabhala[1], Liqun He[1], Yuncheng Man[1,3], Sven B. Spörri[1], Supriya Gharpure[1], Abdul Rahman Isaacs[1], Shay Ferdosi[4], Andrzej S. Pitek[4], Giulietta Maruggi[4], Sylvie Bertholet[4], Jessica Firestone[4], Kambiz Mousavi[4], Eric Miller[4], Kate Luisi[4], Caleb A. Hellman[5], LaTonya D. Williams[5], Georgia D. Tomaras[5], Peng Yin[1,6], Steven P. Gygi[2], Josie McAuliffe[4], Donald E. Ingber[1,3,7*], Girija Goyal[1*]

[1]Wyss Institute for Biologically Inspired Engineering, Harvard University, Boston, MA 02215, USA
[2]Department of Cell Biology, Harvard Medical School, Boston, MA 02115, USA
[3]Vascular Biology Program and Department of Surgery, Boston Children's Hospital and Harvard Medical School, Boston, MA 02115, USA
[4]GSK, Rockville Center for Vaccine Research, Rockville, MD 20850, USA
[5]Center for Human Systems Immunology, Departments of Surgery and Integrative Immunobiology, Duke University School of Medicine, Durham, North Carolina 27701, USA
[6]Department of Systems Biology, Harvard Medical School, Boston, MA, USA
[7]Harvard John A. Paulson School of Engineering and Applied Sciences, Cambridge, MA 02139, USA
*Correspondence: Girija Goyal, Ph.D. (girija.goyal@wyss.harvard.edu), Donald E. Ingber, M.D., Ph.D. (don.ingber@wyss.harvard.edu)

Summary

Predicting the efficacy and toxicity of intramuscular mRNA vaccines remains challenging. Here, we describe an *ex vivo* human cell-based model that replicates immune responses to lipid nanoparticle (LNP)-based mRNA vaccines that require intramuscular injection. Vaccines are administered into a biomimetic muscle module containing human skeletal myoblasts and antigen-presenting cells (APCs) to mimic intramuscular vaccination, followed by transfer of the APCs and soluble factors to a microfluidic human lymphoid

follicle chip (LF Chip) to mimic lymphatic drainage. Non-replicating mRNA vaccines directly induce antigen expression in APCs, whereas self-amplifying mRNA vaccines require muscle cell-APC contact within the intramuscular vaccination module. Transfer of APCs and soluble factors to the LF Chip induces LF expansion, *de novo* antigen-specific IgG production against a naïve antigen (rabies virus glycoprotein), and cytokine release, with responses varying depending on LNP type. Vaccination of LF chips against SARS-COV-2 Spike recall antigen using the Moderna Spikevax vaccine generates neutralizing antibodies and induces somatic hypermutation. This biomimetic platform offers an all-human alternative for evaluating vaccine-induced immunity, potentially obviating the need for non-human primates and accelerating vaccine development.

Introduction

mRNA vaccines have been essential in controlling the COVID-19 pandemic[1,2]. The Moderna and BioNTech mRNA vaccines against COVID-19 comprise uridine-modified, non-replicating mRNAs that encode SARS-CoV-2 spike proteins. Recently, a self-amplifying mRNA (SAM) vaccine that provides equivalent protection to non-replicating mRNA vaccines but at 6-20-fold lower doses was also approved[3–7], further highlighting the potential of mRNA vaccine technology. However, the mechanisms underlying vaccine efficacy and toxicity have been primarily studied in inbred mice and non-human primates (NHPs), which often exhibit immune responses that differ from those seen in humans[8,9]. Furthermore, there has been an extreme shortage of NHPs for vaccine testing since the COVID-19 pandemic[10], and testing in animals, particularly in NHPs, also raises major ethical concerns.

Although animal models have historically dominated FDA approval processes, the FDA's new 2.0 approval pathway now expands the use of human *in vitro* data, including results generated using microfluidic human organ-on-a-chip (Organ Chip) technology, in investigational new drug (IND) applications for regulatory approval[11–13]. Despite this advance, the field of vaccine

56 development has been slow to adopt human cell-based models. Lymphoid organoids and Organ
57 Chip methods using human peripheral blood mononuclear cells (PBMCs) and tonsil cells have
58 been employed for vaccine testing in academic laboratories[14–18]; however, these systems
59 primarily focus on immune memory responses to influenza and COVID-19 vaccines and, most
60 importantly, they have not been able to replicate clinically relevant immune responses that are
61 generated at the injection site.

62 Antigen uptake, distribution, and innate immune responses are all critical factors that must
63 be assessed to define the efficacy of mRNA vaccines[19]. However, unlike protein subunit or
64 inactivated virus vaccines, mRNA vaccines require cellular uptake and intracellular translation of
65 the antigen from the injected mRNA. Lipid nanoparticles (LNPs) are commonly used to
66 encapsulate the mRNAs to promote mRNA uptake and antigen expression in human tissues, and
67 they also may serve as adjuvants to enhance immune responses[20–23]. Consequently, there is a
68 pressing need for human-relevant preclinical models that can more accurately study the
69 mechanism of action of LNP-based mRNA vaccines, as well as their efficacy, toxicities, and
70 associated biomarkers.

71 Most mRNA vaccines are administered through intramuscular injection. Antigen
72 production at the muscle injection site after mRNA vaccine injection quickly peaks after 4–24
73 hours and then gradually wanes, and the release of pro-inflammatory cytokines such as IL-1β and
74 IL-6 may also be important for the vaccine effects[19,24–26]. In this study, we expanded the
75 functionality of our previously published microfluidic organ-on-a-chip model of the human
76 lymphoid follicle (LF Chip)[16] by combining it with a two-dimensional (2D) human intramuscular
77 injection simulation module in which human skeletal myoblast cells (HSMCs) are cultured with
78 antigen-presenting cells (APCs) — either monocytes or dendritic cells (DCs) — and then exposed
79 to LNP-based mRNA vaccines *in vitro*. This module provides a method for detecting the
80 expression of antigens encoded by mRNA vaccines and innate immune responses at the

81 intramuscular vaccination site. By transferring cells and released factors from the intramuscular
82 injection module to the LF Chip, adaptive immune responses can then be captured by measuring
83 the formation of germinal center-like LFs, cytokine release, and antibody production.

84 Here, we used this method to compare immune responses and signaling pathways
85 triggered by non-amplifying and self-amplifying mRNA (SAM) vaccines, as well as different LNP
86 formulations. The method successfully modeled immune responses induced by SAM vaccines
87 against rabies virus glycoprotein, which is a naïve antigen for most United States-based donors.
88 Somatic hypermutation and production of cross-reactive antibodies against various SARS-CoV-
89 2 variants with neutralization activity were also detected when the Moderna bivalent COVID-19
90 mRNA vaccine was administered to this *ex vivo* intramuscular vaccine model.

91

92 ## *Results*

93 ### *Contact between APCs and HSMCs is required for modeling intramuscular vaccination*

94 Monocytes are known to infiltrate vaccine injection sites, take up SAM vaccines, express
95 the antigens, and transport them to the lymph nodes[19,21,27,28]. To explore modeling of
96 intramuscular vaccination with a naïve antigen, we introduced a SAM vaccine encoding Rabies
97 Virus Glycoprotein (RABV-G) and green fluorescent protein (GFP) encapsulated in an LNP (SAM-
98 LNP1) into cultures of primary human monocytes or monocyte-derived DCs either when grown
99 alone or co-cultured with HSMCs **(Fig. 1a)**. Non-toxic doses (1 to 100 ng/mL; **Supplementary**
100 **Fig. 1a,b**) of SAM-LNP1 did not drive reporter expression (GFP) in monocyte monocultures (as
101 assessed by flow cytometry), implying that the antigen was not expressed (**Fig. 1b).** However,
102 when the SAM-LNP1 was added to co-cultures of HSMCs and monocytes **(Fig. 1b, c** and
103 **Supplementary Fig. 1c)** or DCs **(Supplementary Fig. 2a)** to create an intramuscular simulation
104 environment, a dose-dependent increase in GFP expression was detected in both monocytes and
105 DCs suggesting successful antigen expression. While the GFP expression levels were variable
106 between donors **(Fig. 1c, Supplementary Fig. 1c),** the highest level of GFP reporter expression

107 was observed at the 100 ng/mL dose of SAM-LNP1; thus, this dose was used in all subsequent
108 studies.

109 Upon SAM-LNP1 vaccination, increases in levels of multiple inflammatory cytokines were
110 observed in both monocyte monocultures and the combined cultures; however, levels of CCL4,
111 IL-6, and IL-8 were notably higher in the co-culture model when HSMCs were present **(Fig. 1d)**.
112 These cytokines are known to support adaptive immune responses. SAM-LNP1 treatment also
113 increased the expression of CD86 and HLA-DR, which are markers of monocyte and DC
114 activation **(Fig. 1e** and **Supplementary Fig. 2b).** However, CD80 was not induced; CD80 is often
115 upregulated later or under specific conditions, such as prolonged inflammation[22,29]. These results
116 highlight the ability of HSMCs to promote antigen expression and activation of antigen presenting
117 cells and demonstrate the value of the co-culture model.

118 To further investigate the role of HSMCs in antigen expression by APCs, we conducted
119 co-cultures in Transwell™ (TW) inserts with varying pore sizes (0.4, 3, or 8 μm) placed above a
120 HSMC monolayer **(Supplementary Fig. 3a)**. As expected, both untreated and SAM-LNP1
121 vaccinated monocytes were able to migrate from the upper well into the lower chamber containing
122 the HSMCs when they were cultured on filters containing 3 or 8 μm pores, but not the 0.4 μm
123 pore, and vaccinated cells migrated to a greater degree **(Supplementary Fig. 3b)**. Importantly,
124 only vaccinated monocytes that were able to migrate through the larger pores and come in direct
125 contact with the HSMCs displayed expression of GFP-labeled antigen and no antigen reporter
126 expression was observed in monocytes that remained on top of the filter membrane in either the
127 untreated or vaccinated cultures **(Supplementary Fig. 3c)**. These findings indicate that direct
128 cell-cell contact between HSMCs and monocytes is necessary for antigen expression by
129 monocytes vaccinated with SAM-LNP1.

130 ***Mimicking vaccine drainage to lymph nodes from muscle using linked human LF Chips***

131 To mimic the drainage of the vaccine and migration of monocytes from the vaccine site to
132 the lymph node, we removed the conditioned medium from the co-culture of monocytes and

133 HSMCs and flowed it through the top flow channel of a 2-channel, human LF Chip microfluidic
134 culture device, which has been previously shown to support self-assembly of germinal center-like
135 structures[16]. The parallel lower channel that is separated from the top channel by a porous
136 membrane contains autologous B and T cells as well as monocytes isolated from the vaccinated
137 intramuscular injection module embedded at a high lymph node-like density within an extracellular
138 matrix gel **(Fig. 2a)**. When we analyzed multiple LF Chips created with cells from a single donor,
139 we found that exposure to conditioned medium and monocytes from SAM-LNP1 vaccinated co-
140 cultures with HSMCs resulted in a significant increase in the number of germinal center-like LFs
141 within the chips (**Fig. 2b**). While IL-2 and IL-4 often must be added to improve T and B cell survival
142 *in vitro*, the addition of IL-2 and IL-4 did not further enhance LF formation or increase their size in
143 this model (**Fig. 2b,c**).

144 Next, we assessed whether the SAM-LNP1 vaccinated LF Chips were able to generate
145 antigen-specific, anti-RABV-G IgG by testing whether the chip outflows could bind to RABV-G-
146 expressing 293T cells (**Supplementary Fig. 4**). Addition of IL-2 and IL-4 increased production of
147 antigen-specific IgG when a single donor was analyzed (**Fig. 2d**). But when we analyzed multiple
148 chips created with cells from 4 different human donors and treated both vaccinated and
149 unvaccinated chips with IL-2 and IL-4, we confirmed again that addition of these cytokines
150 induced an increase in the number of LFs, but no change in size in vaccinated chips (**Fig. 2e**).
151 Furthermore, when we quantified anti-RABV-G IgG levels in chips created with cells from 3 donors,
152 we found that some chips from each donor secreted anti-RABV-G IgG above baseline levels,
153 while others did not **(Fig. 2f)**. Given the high diversity of the human immune repertoire, the
154 variation between chips from the same donor is likely influenced by the presence and persistence
155 of anti-RABV-G B cells. Indeed, when the B cell repertoire (BCR nucleotide sequences) from 2
156 different donors were compared, there was only ~5% overlap **(Supplementary Fig. 5)**. Finally,
157 when we compared the levels of 18 different cytokines in the LF Chip outflows during 28 days of
158 culture, we found that cytokines known to support the germinal center response and B cell

159 differentiation, such as IL-5, IL-6, CCL4, and IFN-γ[19,20,22,30], increased during the first 2 weeks,
160 followed by a subsequent plateau (**Fig. 2g**). Importantly, as these donors likely have never been
161 vaccinated for rabies or been exposed to this antigen previously, these response are *de novo*
162 vaccination responses.

163 ***SAM-LNP1 and Non-Amplifying mRNA-LNP Vaccines Elicit Distinct Immune Responses***

164 Non-amplifying mRNA vaccines, such as the Moderna and Pfizer COVID vaccines, may
165 employ different immunological mechanisms than SAMs, and hence have different efficacies and
166 toxicities. When we treated HSMC cocultures with monocytes or DCs with a non-amplifying, LNP-
167 based mRNA vaccine against RABV-G antigen (NAM-LNP1), we found that, unlike the SAM
168 vaccine, it showed higher antigen expression in DCs compared to monocytes one day after
169 exposure in coculture with HSMC **(Fig. 3a).** Moreover, the overall expression induced by NAM-
170 LNP1 was significantly lower than with the SAM-LNP1 (not shown) even when using a 10 times
171 higher dose (1,000 ng/ml), likely due to its inability to amplify the response. LNPs can affect tissue
172 tropism and reactogenicity of the vaccine cargo. Thus, we also tested another LNP (LNP2) and
173 found that the same NAM vaccine formulated in LNP1 or LNP2 exhibited different levels of antigen
174 presentation in DCs **(Fig. 3b)**.

175 To test whether SAM-LNP1 vaccination (100 ng/ml) using DCs as APCs would be
176 sufficient to induce anti-RABV-G IgG, we transferred the DC of 2 donors and the outflows from
177 the HSMC cocultures to 3-4 LF Chips per donor and treated the chips with IL-2 and IL-4 as
178 described above. We detected anti-RABV-G IgG in the effluents of two-thirds of the chips when
179 SAM-LNP1 was tested using DCs as the APC. NAM-LNP1 and NAM-LNP2 (1,000 ng/ml) also
180 induced the production of anti-RABV-G IgG compared to empty LNPs, although the levels were
181 modest compared to those induced by SAM-LNP1 **(Fig. 3c)**. The induction of inflammatory
182 cytokines by NAM-LNP1 and NAM-LNP2 also was significantly lower compared to SAM-LNP1,
183 both during the first day of 2D culture and after 14 days in LF Chips **(Fig. 3d,e)**.

184 We then performed quantitative mass spectrometry to compare the proteomic responses
185 induced by NAM-LNP1 (1,000 ng/ml) versus SAM-LNP1 (100 ng/ml) in immune cells extracted
186 from vaccinated LF chips. Proteomic analysis revealed that SAM-LNP1 caused distinct and
187 broader perturbations in the host proteome compared to NAM-LNP1 **(Fig. 4a)**. Eight proteins were
188 downregulated by both SAM and NAM. Among these were H1.4 and H1.5 that are critical for
189 chromatin compaction and which have been reported to influence immune cell differentiation by
190 modulating multiple signaling pathways[31,32]. There were no common upregulated proteins
191 between SAM and NAM-treated LF chips, suggesting significant differences in the pathways
192 altered by SAM and NAM vaccines.

193 SAM-LNP1 predominantly affected proteins involved in antiviral defense and cytokine
194 production regulation **(Fig. 4b)**, strongly upregulating interferon response proteins, particularly
195 members of the antiviral oligoadenylate synthase (OAS) [33] and interferon-induced proteins with
196 tetratricopeptide repeats (IFIT)[34] families. This is consistent with cellular sensing of replicating
197 RNA. While OAS protein expression is variable, IFIT proteins are typically expressed at low levels
198 in healthy cells and are strongly induced upon interferon exposure or viral infection. Similarly,
199 myxovirus resistance (MX) proteins, which are antiviral proteins induced by viral infection[35], were
200 significantly upregulated by SAM-LNP1. Additionally, SAM vaccines induced the expression of C-
201 C motif chemokine receptor 2 (CCR2), which plays a key role in the maturation of antigen-
202 presenting cells[36] and their trafficking to draining lymph nodes[37] via the expression of C-C motif
203 ligand 2 (CCL2, also known as monocyte chemoattractant protein 1, MCP-1). IL-2, crucial for the
204 early priming and activation of T cells[38,39], was also significantly induced by SAM vaccines.

205 In contrast, NAM-LNP1 induced only modest proteomic changes compared to the empty
206 LNP group **(Fig. 4c, Supplementary Fig. 6)**, consistent with the significantly lower mRNA levels[40]
207 in the NAM versus SAM groups. Notably, the proteins upregulated by NAM-LNP1 are closely
208 associated with T cell responses. Among them, Kinase Suppressor of Ras 1 (KSR1), a scaffold
209 protein, plays a crucial role in regulating the activation threshold of Extracellular Signal-Regulated

210 Kinase (ERK) in T cells[41,42]; Unc-13 Homolog D (UNC13D) is essential for mediating the release
211 of cytolytic granules from T cells[43]; and Fatty Acid Binding Protein 4 (FABP4) is involved in
212 modulating T cell receptor signaling pathways[44].

213 ***Somatic hypermutation induced by mRNA-LNP vaccines.***

214 To study the recall responses of mRNA vaccines in this LF Chip-based intramuscular
215 vaccination platform, we used the Moderna Spikevax bivalent Original and Omicron BA.4/BA.5
216 vaccine and conducted experiments using both DCs and monocytes from vaccinated HSMC
217 cocultures as well as conditioned medium along with IL-2 and IL-4, using the linking method
218 described above. This vaccine was chosen because its induction of neutralizing antibodies has
219 been well-documented in humans, and somatic hypermutations (SHMs) often require multiple
220 vaccine exposures [45]. In multiple LF chips created from the cells of 4 different donors, vaccination
221 using the Moderna mRNA vaccine (500 ng/ml) induced robust IgG responses against the SARS-
222 CoV-2 Wuhan strain, as well as the Omicron BA.4 and BA.5 variants. The IgG titer in unvaccinated
223 and vaccinated chips against the Wuhan spike was 3 to 10 times higher than the titer against the
224 BA.4 and BA.5 spikes **(Fig. 5a),** which may reflect the wide distribution of the monovalent vaccines
225 against the Wuhan strain within Massachusetts where our immune cell donor pool is located. We
226 also verified the neutralization efficiency of the antibodies produced by the LF Chips from 2 donors
227 **(Fig. 5b)** by testing the ability of the chip outflows to block infection of ACE2-expressing 293T
228 cells by a pseudovirus expressing the Wuhan strain spike protein.

229 To understand whether the variable neutralization efficiency of the induced antibodies in
230 the outflow from different chips and donors **(Fig. 5b)** reflects a lack of B cell activation and
231 maturation or the detection limits of our workflow, we sequenced the CDR3 loop of the IgH locus
232 from cells isolated from the LF Chips from 2 donors 14 days after vaccination. Due to the diversity
233 of the human immune repertoire and the limited overlap between chips from the same donor,
234 sequences from 3 chips for each donor were pooled for further analysis; over 100,000 unique
235 sequences were obtained per donor (**Fig. 5c**). Both donors showed an increase in the total

236 number of B cell sequences, unique sequences, B cells with SHMs, and total SHMs upon
237 vaccination. However, donor 2, which produced higher levels of neutralizing antibodies, had more
238 B cells with existing mutations, and yet a significant increase in SHM was still observed upon
239 vaccination; vaccination did not alter V, D, or J gene usage (data not shown).

240 The top 10 V-D-J combinations had >100 mutations in the LF Chip even without
241 vaccination, which indicates the baseline diversity of the donor BCR repertoire, but vaccination
242 resulted in 5-10% increase in SHMs in donor 2 (**Fig. 5d**), and a similar trend was observed in
243 donor 1. We found that vaccinated chips had a higher average level of SHMs as clone size
244 increased **(Fig. 5e)**, a pattern evident in both donors, and donor 2 had larger clones than donor
245 1. To look at these effects in greater detail, we compared sequences from specific, highly
246 expanded V-D-J combinations between vaccinated and unvaccinated chips. As shown for a
247 representative V-D-J combination from donor 2 (**Fig. 6)**, vaccination increased the number of
248 mutated sequences and the number of mutations in expanded clones, confirming that the LF chip
249 displays SHM upon stimulation with vaccines.

250

251 ***Discussion***

252 The efficacy of mRNA vaccines is closely tied to the mRNA format, delivery vehicle, and route
253 of administration[19,46,47]. In this study, we developed an *ex vivo* model mimicking the intramuscular
254 injection site and combined it with LF Chips to create an experimental platform that provides a
255 comprehensive view of mRNA vaccine uptake and immune responses in humans. We observed
256 that the expression of antigen encoded by SAM vaccine in the APCs depends on co-culture with
257 muscle cells and the formation of direct cell-cell contacts. This co-culture also enhanced the
258 activation of APCs in response to mRNA vaccination, as indicated by increased expression of
259 surface markers (e.g., CD86, HLA-DR), and the release of pro-inflammatory cytokines, including
260 IL-6 and IL-8. Interestingly, IL-6, a key regulator of T follicular helper cells[48–50], was specially
261 induced by SAM vaccines when APCs were co-cultured with muscle cells. These findings

262 emphasize the importance of studying vaccine distribution, innate immune responses, and the
263 contribution of stromal cells to responses, particularly to SAM vaccines, as previously noted by
264 others[51,19,52,45,53]. In contrast, NAM vaccines can be taken up directly by monocytes and DCs in
265 the absence of muscle cells; however, the LNP component affects cytokine release and antigen
266 expression[17,21,51,54].

267 To detect adaptive immune responses induced by mRNA vaccines, we mixed APCs from
268 the intramuscular vaccination simulation module with autologous T and B cells to create an LF
269 Chip model of a draining lymph node, leveraging our published method[16]. The conditioned
270 medium from the intramuscular vaccination module containing released soluble factors was also
271 transferred to the top channel of the LF Chip. Notably, we found that SAM vaccines induce LF
272 formation, and the addition of IL-2 and IL-4 enhances antigen-specific antibody production,
273 although it does not further alter the number or size of the LFs. These LF Chips can be maintained
274 for up to 28 days in culture, allowing for the long-term study of cytokine release induced by mRNA
275 vaccines. The secreted cytokines we detected, including IL-1α, IL-1β, IL-6, and CXCL10, are
276 consistent with findings from previous *in vivo* studies of SAM vaccines[20,22,23,30]. Our experiments
277 also confirm that the LF Chip supports immunoglobulin G generation when challenged with naïve
278 antigens, a capability lacking in other systems that utilize blood-derived cells[17,18]. Notably, only
279 approximately 0.0055% to 0.088% of B cells in peripheral blood bind RABV-G[55]. Given that
280 Rabies patients were excluded from our donor pool and that RABV-G shares only ~20% sequence
281 identity even with other rhabdoviruses[56], the responses observed in the chips likely originate from
282 naïve B cells.

283 Comparing multiple LNP delivery vehicles and RNA payload types opens opportunities for
284 *in vitro* comparative studies to identify optimal combinations of delivery vehicles and mRNA
285 formats. Our on-chip study confirmed previous reports that SAM vaccines can induce similar
286 immune responses at doses 10 times lower than those required for NAM vaccines[57]. Interestingly,
287 while the cytokine induction patterns of the three mRNA vaccines tested were similar, SAM

288 vaccines triggered significantly more robust cytokine responses and antigen-specific antibodies
289 than NAM vaccines. This may be related to our finding from our proteomic analysis, which
290 revealed that SAM and NAM vaccines activate distinct signaling pathways. Of the proteins altered
291 differently by SAM and NAM vaccines, only 8 overlapped between the 2 vaccine formats, with 83
292 unique proteins induced by the SAM and 60 by NAM vaccines. SAM vaccines appeared to
293 activate more robust viral defense and cytokine regulation pathways. To our knowledge, this is
294 the first reported proteomic comparison of human immune cell proteome changes induced by
295 different mRNA vaccine formats, and we anticipate that further studies of vaccine-induced
296 signaling pathways will provide valuable insights for future vaccine design.

297 We also tested the Moderna bivalent COVID-19 mRNA vaccine to investigate memory
298 responses and booster effects using our method for modeling intramuscular vaccination. Since
299 most of our immune cell donors had likely received a COVID-19 mRNA vaccine due to state
300 policies in Massachusetts, we anticipated observing memory immune responses against the
301 SARS-CoV-2 antigen contained with this vaccine in cells from these donors. Our results were
302 consistent with previous findings, showing that the bivalent COVID-19 mRNA vaccine induced 3-
303 10 times more antibodies against the Wuhan strain compared to the Omicron BA.4 and BA.5
304 variants[58,59]. Also, the neutralizing efficacy of the antibodies produced by the LF Chip platform
305 was confirmed, and SHM analysis revealed that B cells underwent SHM within the chip
306 environment. This is also the first report of inducing somatic hypermutation in blood-derived B
307 cells *in vitro* with a clinical mRNA vaccine.

308 In conclusion, this study establishes a robust method for interrogating human immune
309 responses to mRNA-LNP vaccination at both the vaccine injection site and within lymphoid tissues.
310 In contrast to previous methods that primarily focused on memory responses[15–18], this preclinical
311 model is capable of evaluating both *de novo* and memory human B cell responses to multiple
312 mRNA vaccine formats. We also characterized the dynamics of cytokine release and antibody
313 production associated with different mRNA vaccine modalities, which can be further leveraged to

314 profile *in vivo* immune responses during clinical trials. While this study primarily focused on
315 cytokine release and B cell responses, future work could expand on these findings by
316 investigating antigen-specific T cell responses. Additionally, this system could be used to study
317 the roles of other immune cells during vaccination, such as mast cells, plasmacytoid dendritic
318 cells, and natural killer cells. Further refinements could include adding stromal cells to the
319 intramuscular module to accurately represent the complexity of the injection site, as fibroblasts
320 and other stromal cell types play a crucial role in antigen uptake and innate immune
321 responses.[60,61] Most importantly, these data demonstrate that this experimental model of human
322 vaccination offers a new and exciting alternative to NHP studies in future vaccine development
323 programs.

324 STAR★Methods

325 Expansion of HSMCs

326 HSMCs (Lonza, CC-2580) were rapidly thawed in a water bath and resuspended in Skeletal
327 Muscle Growth Medium-2 (SkGM-2, Lonza, CC-3245). Cells were seeded in a T-150 flask for
328 expansion. Confluency and morphology were monitored daily using brightfield microscopy, and
329 media were changed every three days. Cells were used for vaccination experiments upon
330 reaching 70-80% confluency.

331 Peripheral Blood Mononuclear Cells (PBMC) Isolation and DC Differentiation

332 De-identified human patient-derived apheresis collars were obtained from the Crimson
333 Biomaterials Collection Core Facility, under Institutional Review Board approval from Harvard
334 University (protocol 22470). PBMCs were isolated by density centrifugation using Lymphoprep
335 (StemCell Technologies, 07801), followed by magnetic bead-based negative selection for B cells
336 (StemCell Technologies, 19054), T cells (17951), and monocytes (19058). For cryopreservation,
337 cells were frozen in Recovery Cell Culture Freezing Medium (Gibco, 12648-010) at 20 million

338 cells/mL. Monocytes were differentiated into DCs by culturing in complete RPMI with 400 ng/mL
339 GM-CSF (Mitenyi Biotec, 130-095372) and 250 ng/mL IL-4 for 5-6 days, with 50% medium
340 replacement every 2 days.

341 **Rabies Virus Glycoprotein and Enhanced Green Fluorescent protein (eGFP) mRNA**
342 **Preparation**

343 The antigen sequence of the full-length Rabies Virus Glycoprotein is based on the Pasteur strain
344 (GenBank accession number: AAA47218.1). The Open Reading Frame (ORF) was optimized for
345 expression in mammalian cells and cloned into SAM or mRNA backbones using standard
346 molecular biology techniques. In the SAM construct, the Rabies G gene was cloned in the first
347 position and the eGFP (GenBank AAB02572) second, separated by the IRES from Enterovirus
348 71 (EV71). In vitro RNA transcription, purification, and LNP formulation were performed as
349 described previously[62–64]. Tri-link prepared conventional mRNA with the same Rabies Virus
350 Glycoprotein sequence, incorporating n-1-methyl-pseudouridine in place of uridine.

351 **LNP Formulation Preparation**

352 Lipid and RNA components were prepared in ethanol and citrate buffer, respectively. LNPs
353 encapsulating RNA were formulated by lipid nanoprecipitation using a modified ethanol dilution
354 process. After the formation of the LNP, the LNP was buffer exchanged using a desalting column
355 into a holding buffer. A sucrose excipient was added to the LNPs for final storage.

356 **Co-culture of Muscle Cells and Antigen-Presenting Cells (APCs) with Vaccination**

357 Skeletal muscle cells were trypsinized using 0.05% trypsin-EDTA (Gibco, 25300054),
358 resuspended in SkGM-2 medium, and seeded at a density of 120,000 cells per well in a 24-well
359 plate. Cells were incubated overnight to allow for adherence. Monocytes were thawed, or cultured
360 dendritic cells (DCs) were collected and resuspended at a concentration of 0.5 million cells/mL,

361 and 0.5 million monocytes or DCs were added to the muscle cell wells along with the indicated
362 mRNA vaccine.

363 **Human LF Chip**

364 Two-channel microfluidic Organ Chip devices and ZOE-ORB instruments were obtained from
365 Emulate Inc. The Organ Chips were plasma-activated and seeded as previously described[16].
366 Briefly, chips were perfused with 1% 3-Aminopropyltrimethoxysilane (Sigma, 281778) in ethanol
367 for 1 hour, followed by washing the channels with ethanol. Chips were incubated in an 80°C oven
368 overnight. For muscle-APC co-culture experiments, media were collected and pooled, and cell
369 counts were performed. For RABV-G mRNA vaccine experiments, APCs were mixed with T and
370 B cells at a 5 : 47.5 : 47.5 ratio to achieve a final concentration of 1.5 × 10^8 cells/mL in complete
371 RPMI supplemented with Matrigel (60%; Corning, 356234) and type I collagen (15%; Corning,
372 354249). For COVID-19 mRNA vaccine experiments, DCs and monocytes from muscle co-
373 cultures were mixed with T and B cells in a 1:1:49:49 ratio. A 15 µL aliquot of the cellularized ECM
374 mixture was introduced into the bottom channel of the 2-channel Organ Chip. After allowing the
375 matrix to gel for 30 minutes at 37°C, the top channel was filled with conditioned medium, prepared
376 as a 1:2 ratio of co-culture to fresh media for RABV-G mRNA vaccines, and a 1:1:8 ratio of DC
377 co-culture medium, monocyte co-culture medium, and fresh media for COVID-19 mRNA vaccines.
378 The chips were perfused with indicated media at 40 µL/h using ZOE instruments in a 37°C
379 incubator.

380 **Immunostaining and Imaging**

381 Chips were fixed by adding 200 µL of 4% paraformaldehyde to one side and allowing 30-50 µL to
382 flow out. Both ports were then plugged, and an additional 200 µL was added. After 1 hour of
383 rocking at room temperature to facilitate back and forth flow of paraformaldehyde solution in the
384 channel, chips were washed twice with PBS for 15 minutes. Nuclear staining was performed using

385 Hoechst (1:1000 dilution, Invitrogen, H3570) for 1 hour, followed by three 15-minute PBS washes.
386 Imaging was performed on a Leica SP5 confocal microscope, and follicle size and number were
387 quantified using Imaris software (Bitplane, version 9.3).

388 For imaging vaccinated HSMC in Supplementary Figure 1c, HSMC vaccinated for 24 hours in a
389 96-well plate were imaged with a Sapphire Biomolecular Imager (Azure Biosystems) and
390 analyzed using Sapphire software (V1.12.0921.0). In Figures 4a, co-cultured vaccinated APCs
391 were immunostained with anti-Rabies-G (Millipore Corp, MAB8727, 1:1000) and goat anti-mouse
392 IgG (H&L) Cross-Adsorbed Secondary Antibody (Invitrogen, A-21235, 1:2000). Images were
393 taken with an ImageXpress Micro4 (Molecular Devices) and analyzed using MetaXpress
394 (6.5.3.427) and ImageJ software (v 2.14.0)

395 **Extraction of Live Cells from Organ Chips**

396 The gel from the bottom channel of the LF chip was collected in Cell Recovery Solution (Corning,
397 354253). The collection tube was centrifuged at 300g for 5 minutes, and the supernatant was
398 aspirated. The pellet was resuspended in 1 mL of fresh Cell Recovery Solution and incubated on
399 ice for 1 hour. Following incubation, the sample was centrifuged again at 300g for 5 minutes, the
400 supernatant was aspirated, and the cells were prepared for downstream applications.

401 **Flow cytometry**

402 Cell viability was assessed using ViaKrome 808 Fixable Viability Dye (Beckman Coulter, C36628,
403 1:100 dilution). Cells were stained with antibodies for CD14 (BD 563561), CD1c (BioLegend
404 331526), HLA-DR (BioLegend 361610), CD80 (BioLegend 305231), CD86 (BioLegend 305430),
405 anti-Rabies-G (Millipore Corp, MAB8727) and goat anti-mouse IgG (H&L) Cross-Adsorbed
406 Secondary Antibody (Invitrogen, A-21235). Data were collected on a CytoFlex LX (Beckman
407 Coulter) and analyzed using FlowJo V10 software (FlowJo LLC).

408 **Cell-Based Assay for Anti-Rabies Antibody Detection**

409 293T cells (1 x 10^6) were seeded in 6-well plates in DMEM with 10% FBS and 1% P/S, 48 hours
410 prior to transfection. Cells were transfected with 50 ng/mL of SAM-RABV-G-GFP-LNPs or empty
411 LNPs (control) and incubated in 2 mL of serum-free DMEM. We used the SAM vaccine to make
412 RABV-G expressing 293T. Cells were incubated with outflows to be tested for anti-RABV-G
413 antibodies and then cells stained with ViaKrome 808 dye and anti-human IgG APC (Biolegend
414 410712). Differential staining with anti-human IgG of control vs. RABV-G expressing 293T
415 indicated the presence of anti-RABV-G antibodies. Specific binding was calculated as shown in
416 **Supplementary Fig. 4**.

417 **Proteome Analysis by Mass Spectrometry**

418 The mass spectrometry-based multiplexed proteomic analysis was performed as previously
419 described[65]. Briefly, human immune cells were cultured for two weeks at LF chips with different
420 mRNA vaccines. The cells were then lysed in 8 M urea and 200 mM EPPS pH 8.5 with Pierce
421 Protease and Phosphatase Inhibitor (Thermo Fisher, A32961). Protein concentration was
422 measured by BCA assay. ~20 µg proteome in 20 µL was treated sequentially with 20 mM TCEP
423 and 200 mM IAA for 15 minutes and 30 minutes, respectively. 3 µL SP3 beads (1:1 mixture of
424 hydrophobic and hydrophilic type, 50 mg/mL, (Cat. #45152105050250 and Cat.
425 #65152105050250) and 30 µL ethanol supplemented with 20 mM DTT were added to the lysate.
426 SP3-bind proteome was washed twice with 80% Ethanol followed by sequential digestion with 0.2
427 µg Lys-C and 0.2 µg trypsin for 2 hours and overnight at 37 °C, respectively. The digested
428 peptides were added 10 µL acetonitrile and labeled with 4 µL TMTpro reagent for 1 hour before
429 combining all samples into one single multiplexed sample and desalting through Sep-Pak C18
430 column. The eluent was dried and then fractionated by basic-pH HPLC for total 24 fractions.

431 Both fractionated proteome samples were analyzed by liquid chromatography-tandem mass
432 spectrometry (LC-MS/MS) on an Orbitrap Eclipse mass spectrometer coupled to a Proxeon

433 NanoLC-1200 UHPLC50 and FAIMS Pro device. Data were collected alternating between a set
434 of three FAIMS compensation voltages (CVs) at -40, -60, and -80 V was used. MS1 scans were
435 collected in the Orbitrap with a resolution setting of 60 K for proteome, a mass range of 400-1600
436 m/z, an AGC at 100%, and a maximum injection time of 50 ms. MS2 scans were acquired in Top
437 Speed mode with a cycle time of 1 s. Peptide precursors were selected and fragmented using
438 HCD with a collision energy of 36. MS2 scans were collected in the Orbitrap with a resolution of
439 50K, a fixed scan range of 110-2000 m/z, and a 500% AGC with a maximum injection time of 86
440 ms. Dynamic exclusion was set to 90 s with a mass tolerance of ± 10 p.p.m.

441 The mass spectra were processed using a Comet-based pipeline and searches were performed
442 using a 50-ppm precursor ion tolerance for the analysis of the total protein levels[66]. The product
443 ion tolerance was set to 0.9 Da. Tandem mass tags on lysine residues and peptide amino termini
444 (+304.2071 Da) and carbamidomethylation of cysteine residues (+57.021 Da), were set as static
445 modifications, whereas oxidation of methionine residues (+15.995 Da) was set as a variable
446 modification. Peptide-spectrum matches were adjusted to a 1% false-discovery rate[67]. Proteins
447 were quantified by summing the reporter-ion counts across all matching peptide-spectrum
448 matches, as described previously. Gene Ontology analysis and graphs was generated using R
449 packages ClusterProfiler[68], Complexed Heatmap and Ehanced Volcano.

450 **Proteomic Data Availability**

451 The mass spectrometry data have been deposited at the ProteomeXchange Consortium and are
452 publicly available as of the date of publication. The accession number is PXD056699. (The
453 reviewer access can be provided if required during submission.)

454 **Immunoglobulin and Cytokine Quantification**

455 To measure immunoglobulins targeting multiple SARS-CoV-2 spike protein variants in the day 9
456 outflow from both unvaccinated and vaccinated LF chips, the Meso Scale Discovery (MSD) V-

457 PLEX SARS-CoV-2 Spike Panel 27 (IgG) Kit (K15437U) was used, with data acquired on an MSD
458 Meso Sector S 600 microplate reader and analyzed with Discovery Workbench 4.0 software. The
459 MSD V-PLEX SARS-CoV-2 Spike Panel 27 (IgG) Kit included 96-well plates immobilized with
460 Wuhan, BA.4, and BA.5 spike antigens (data reported in Fig. 6a), along with a beta variant
461 (B.1.351), delta variant (B.1.617.2; AY.4 Alt Seq 2) and additional omicron sub-lineage spike
462 proteins (BA.2, BA.2.12.1, BA.2+L452M, BA.2+L452R, and BA.3; data not shown), in addition to
463 a reference standard and three controls with known levels of antibodies against antigens in the
464 kit. Assays were performed following the MSD-provided, kit-specific protocol, testing LF chip
465 outflows in duplicate and including CH65 IgG monoclonal antibody (mAb) (influenza receptor
466 binding site-specific mAb) as a negative control. Data from LF chip outflow dilutions (1:10, 1:70,
467 1:490) falling nearest to the midpoint of the accurate range of the standard curve were selected
468 for reporting. Values chosen were back calculated against the standard curve and reported as
469 arbitrary units per milliliter (AU/mL), accounting for dilution factor.

470 The cytokine levels in the media were assessed using a custom MSD kit (as presented in **Figures**
471 **1d** and **3d,e**) and read using an MSD microplate reader model 1300 alongside the Discovery
472 Workbench 4.0 software. Customized Luminex® Multiplex Assay kits from Thermo Fisher
473 Scientific were employed for the cytokine concentrations in the effluents depicted in **Figure 2g**.
474 Analyte concentrations were determined on a Bio-Plex 3D suspension array system, and the
475 standard curve fitting and concentration calculations were conducted using Bio-Plex Manager
476 software (Bio-Rad, version 6.0).

477 **BCR Nucleotide Sequences Analysis**

478 Human immune cells were cultured on LF chips for two weeks with 500 ng/ml of the Moderna
479 bivalent COVID-19 mRNA vaccine. Following this, cells were extracted from the chips and sent

480 to Adaptive Biotechnologies for sequencing of the CDR3 loop of IgH. The data was then analyzed
481 and visualized using the immunoSEQ Analyzer, Clustal W[69], iTOL[70] and pivot charts in Prism 10.

482 **Statistics**

483 All experiments (excluding proteomics) were performed at least twice, with at least three technical
484 replicates for each group in each experiment. Data are presented as mean values ± standard
485 deviation (SD). Graphing and statistical comparisons were carried out using GraphPad Prism
486 software (v10.1.0). Statistical significance for comparisons between two groups was determined
487 using an unpaired t-test. A P-value of <0.05 was considered statistically significant, with exact P-
488 values labeled in all figures.

489

490 **Acknowledgments**

491 The studies on SAM and NAM vaccines were sponsored by GSK. The studies with Moderna
492 vaccines and on somatic hypermutation were supported by funding from the Bill and Melinda
493 Gates Foundation (INV-002274 to G.G. and D.E.I) and the in-kind Women in Science Award from
494 Adaptive Biotechnologies (to G.G.), Development of the LF chip was also supported by funding
495 from the Bill and Melinda Gates Foundation (INV-002164 to D.E.I), the Biomedical Advanced
496 Research and Development Authority (contract 75A50121C00075 to D.E.I) and the Biomedical
497 Advanced Research and Development Authority-U.S. Food and Drug Administration (contract
498 75A50123D00004 to D.E.I), SARS-CoV-2-specific IgG antibody quantification in organ-chip
499 outflows supported by funding from Gates Foundation (INV-060822 to G.D.T.), as well as by a
500 Wyss Technology Development Fellowship (to Y.Z.). The authors would like to thank Harvard
501 University Health Services for sharing the unused portion of the Moderna vaccine from opened
502 vials to enable the studies on the production of neutralizing antibodies and somatic hypermutation.

503

504 **Author contributions**

505 Y.Z., J.M., D.E.I, and G.G. conceived the study. J.M., D.E.I, and G.G. oversaw the study. Y.Z.,
506 M.W.K., K.Y., L.H., S.F., A.S.P., G.M., S.B., K.L., C.A.H., L.D.W., G.D.T., P.Y., S.G., J.M., D.E.I.,
507 and G.G. participated in experiment design and/or discussions. Y.Z., M.W.K., K.Y., A.P., P.P.,
508 L.H., Y.M., S.S., S.G., A.R.I., J.F., K.M., E.M., C.A.H., and L.D.W. performed the experiments and
509 data collection. Y.Z., M.W.K., K.Y., D.E.I., and G.G. analyzed the data, prepared the figures and
510 tables, and wrote the manuscript with input from all authors. D.E.I. and G.G. reviewed and edited
511 the manuscript. All authors approved the final version.

512 **Competing interests**

513 D.E.I. is a founder, board member, scientific advisory board chair, and equity holder in Emulate,
514 Inc.; D.E.I. and G.G. are co-inventors on relevant patent applications. S.F., A.S.P., G.M., S.B.,
515 J.F., K.M., E.M., K.L., and J.M. are employees of the GSK group of companies and may own GSK
516 shares and/or restricted GSK shares. The other authors declare no other competing interests.

517

518 **REFERENCES**

519 1. Polack, F.P., Thomas, S.J., Kitchin, N., Absalon, J., Gurtman, A., Lockhart, S., Perez, J.L.,
520 Marc, G.P., Moreira, E.D., Zerbini, C., et al. (2020). Safety and Efficacy of the BNT162b2
521 mRNA Covid-19 Vaccine. N. Engl. J. Med. *383*, 2603–2615.
522 https://doi.org/10.1056/NEJMoa2034577.

523 2. Baden, L.R., Sahly, H.M.E., Essink, B., Kotloff, K., Frey, S., Novak, R., Diemert, D., Spector,
524 S.A., Rouphael, N., Creech, C.B., et al. (2021). Efficacy and Safety of the mRNA-1273
525 SARS-CoV-2 Vaccine. N. Engl. J. Med. *384*, 403–416.
526 https://doi.org/10.1056/NEJMoa2035389.

527 3. Dolgin, E. (2023). Self-copying RNA vaccine wins first full approval: what's next? Nature
528 *624*, 236–237. https://doi.org/10.1038/d41586-023-03859-w.

529 4. Oda, Y., Kumagai, Y., Kanai, M., Iwama, Y., Okura, I., Minamida, T., Yagi, Y., Kurosawa, T.,
530 Greener, B., Zhang, Y., et al. (2024). Immunogenicity and safety of a booster dose of a self-
531 amplifying RNA COVID-19 vaccine (ARCT-154) versus BNT162b2 mRNA COVID-19
532 vaccine: a double-blind, multicentre, randomised, controlled, phase 3, non-inferiority trial.
533 Lancet Infect. Dis. *24*, 351–360. https://doi.org/10.1016/S1473-3099(23)00650-3.

534 5. Vogel, A.B., Lambert, L., Kinnear, E., Busse, D., Erbar, S., Reuter, K.C., Wicke, L.,
535 Perkovic, M., Beissert, T., Haas, H., et al. (2018). Self-Amplifying RNA Vaccines Give
536 Equivalent Protection against Influenza to mRNA Vaccines but at Much Lower Doses. Mol.
537 Ther. *26*, 446–455. https://doi.org/10.1016/j.ymthe.2017.11.017.

538 6. Pollock, K.M., Cheeseman, H.M., Szubert, A.J., Libri, V., Boffito, M., Owen, D., Bern, H.,
539 McFarlane, L.R., O'Hara, J., Lemm, N.-M., et al. (2022). Safety and immunogenicity of a
540 self-amplifying RNA vaccine against COVID-19: COVAC1, a phase I, dose-ranging trial.
541 eClinicalMedicine *44*, 101262. https://doi.org/10.1016/j.eclinm.2021.101262.

542 7. Schmidt, C., and Schnierle, B.S. (2023). Self-Amplifying RNA Vaccine Candidates:
543 Alternative Platforms for mRNA Vaccine Development. Pathogens *12*, 138.
544 https://doi.org/10.3390/pathogens12010138.

545 8. Mestas, J., and Hughes, C.C.W. (2004). Of Mice and Not Men: Differences between Mouse
546 and Human Immunology. J. Immunol. *172*, 2731–2738.
547 https://doi.org/10.4049/jimmunol.172.5.2731.

548 9. Pulendran, B., and Davis, M.M. (2020). The science and medicine of human immunology.
549 Science *369*, eaay4014. https://doi.org/10.1126/science.aay4014.

550 10. Wee, S.-L., and Tarnowski, B. (2021). Future Vaccines Depend on Test Subjects in Short
551 Supply: Monkeys. N. Y. Times.

552 11. Han, J.J. (2023). FDA Modernization Act 2.0 allows for alternatives to animal testing. Artif.
553 Organs *47*, 449–450. https://doi.org/10.1111/aor.14503.

554 12. Zushin, P.-J.H., Mukherjee, S., and Wu, J.C. (2023). FDA Modernization Act 2.0:
555 transitioning beyond animal models with human cells, organoids, and AI/ML-based
556 approaches. J. Clin. Invest. *133*, e175824. https://doi.org/10.1172/JCI175824.

557 13. Ingber, D.E. (2022). Human organs-on-chips for disease modelling, drug development and
558 personalized medicine. Nat. Rev. Genet. *23*, 467–491. https://doi.org/10.1038/s41576-022-
559 00466-9.

560 14. Wagar, L.E., Salahudeen, A., Constantz, C.M., Wendel, B.S., Lyons, M.M., Mallajosyula, V.,
561 Jatt, L.P., Adamska, J.Z., Blum, L.K., Gupta, N., et al. (2021). Modeling human adaptive
562 immune responses with tonsil organoids. Nat. Med. *27*, 125–135.
563 https://doi.org/10.1038/s41591-020-01145-0.

564 15. Kastenschmidt, J.M., Sureshchandra, S., Jain, A., Hernandez-Davies, J.E., Assis, R. de,
565 Wagoner, Z.W., Sorn, A.M., Mitul, M.T., Benchorin, A.I., Levendosky, E., et al. (2023).
566 Influenza vaccine format mediates distinct cellular and antibody responses in human
567 immune organoids. Immunity *0*. https://doi.org/10.1016/j.immuni.2023.06.019.

568 16. Goyal, G., Prabhala, P., Mahajan, G., Bausk, B., Gilboa, T., Xie, L., Zhai, Y., Lazarovits, R.,
569 Mansour, A., Kim, M.S., et al. (2022). Ectopic Lymphoid Follicle Formation and Human
570 Seasonal Influenza Vaccination Responses Recapitulated in an Organ-on-a-Chip. Adv. Sci.
571 *9*, 2103241. https://doi.org/10.1002/advs.202103241.

572 17. Jeger-Madiot, R., Planas, D., Staropoli, I., Debarnot, H., Kervevan, J., Mary, H., Collina, C.,
573 Fonseca, B.F., Robinot, R., Gellenoncourt, S., et al. (2024). Modeling memory B cell
574 responses in a lymphoid organ-chip to evaluate mRNA vaccine boosting. J. Exp. Med. *221*,
575 e20240289. https://doi.org/10.1084/jem.20240289.

576 18. Zhong, Z., Quiñones-Pérez, M., Dai, Z., Juarez, V.M., Bhatia, E., Carlson, C.R., Shah, S.B.,
577 Patel, A., Fang, Z., Hu, T., et al. (2024). Human immune organoids to decode B cell
578 response in healthy donors and patients with lymphoma. Nat. Mater., 1–15.
579 https://doi.org/10.1038/s41563-024-02037-1.

580 19. Verbeke, R., Hogan, M.J., Loré, K., and Pardi, N. (2022). Innate immune mechanisms of
581 mRNA vaccines. Immunity *55*, 1993–2005. https://doi.org/10.1016/j.immuni.2022.10.014.

582 20. Alameh, M.-G., Tombácz, I., Bettini, E., Lederer, K., Ndeupen, S., Sittplangkoon, C.,
583 Wilmore, J.R., Gaudette, B.T., Soliman, O.Y., Pine, M., et al. (2021). Lipid nanoparticles
584 enhance the efficacy of mRNA and protein subunit vaccines by inducing robust T follicular
585 helper cell and humoral responses. Immunity *54*, 2877-2892.e7.
586 https://doi.org/10.1016/j.immuni.2021.11.001.

587 21. Hassett, K.J., Rajlic, I.L., Bahl, K., White, R., Cowens, K., Jacquinet, E., and Burke, K.E.
588 (2024). mRNA vaccine trafficking and resulting protein expression after intramuscular
589 administration. Mol. Ther. - Nucleic Acids *35*. https://doi.org/10.1016/j.omtn.2023.102083.

590 22. Li, C., Lee, A., Grigoryan, L., Arunachalam, P.S., Scott, M.K.D., Trisal, M., Wimmers, F.,
591 Sanyal, M., Weidenbacher, P.A., Feng, Y., et al. (2022). Mechanisms of innate and adaptive
592 immunity to the Pfizer-BioNTech BNT162b2 vaccine. Nat. Immunol. *23*, 543–555.
593 https://doi.org/10.1038/s41590-022-01163-9.

594 23. Tahtinen, S., Tong, A.-J., Himmels, P., Oh, J., Paler-Martinez, A., Kim, L., Wichner, S., Oei,
595 Y., McCarron, M.J., Freund, E.C., et al. (2022). IL-1 and IL-1ra are key regulators of the
596 inflammatory response to RNA vaccines. Nat. Immunol. *23*, 532–542.
597 https://doi.org/10.1038/s41590-022-01160-y.

598 24. Gote, V., Bolla, P.K., Kommineni, N., Butreddy, A., Nukala, P.K., Palakurthi, S.S., and Khan,
599 W. (2023). A Comprehensive Review of mRNA Vaccines. Int. J. Mol. Sci. *24*, 2700.
600 https://doi.org/10.3390/ijms24032700.

601 25. Röltgen, K., Nielsen, S.C.A., Silva, O., Younes, S.F., Zaslavsky, M., Costales, C., Yang, F.,
602 Wirz, O.F., Solis, D., Hoh, R.A., et al. (2022). Immune imprinting, breadth of variant
603 recognition, and germinal center response in human SARS-CoV-2 infection and vaccination.
604 Cell *185*, 1025-1040.e14. https://doi.org/10.1016/j.cell.2022.01.018.

605 26. Nitika, Wei, J., and Hui, A.-M. (2022). The Delivery of mRNA Vaccines for Therapeutics. Life
606 *12*, 1254. https://doi.org/10.3390/life12081254.

607 27. Clemente, B., Denis, M., Silveira, C.P., Schiavetti, F., Brazzoli, M., and Stranges, D. (2023).
608 Straight to the point: targeted mRNA-delivery to immune cells for improved vaccine design.
609 Front. Immunol. *14*. https://doi.org/10.3389/fimmu.2023.1294929.

610 28. Maruggi, G., Zhang, C., Li, J., Ulmer, J.B., and Yu, D. (2019). mRNA as a Transformative
611 Technology for Vaccine Development to Control Infectious Diseases. Mol. Ther. *27*, 757–
612 772. https://doi.org/10.1016/j.ymthe.2019.01.020.

613 29. Kennedy, A., Waters, E., Rowshanravan, B., Hinze, C., Williams, C., Janman, D., Fox, T.A.,
614 Booth, C., Pesenacker, A.M., Halliday, N., et al. (2022). Differences in CD80 and CD86
615 transendocytosis reveal CD86 as a key target for CTLA-4 immune regulation. Nat. Immunol.
616 *23*, 1365–1378. https://doi.org/10.1038/s41590-022-01289-w.

617 30. Pepini, T., Pulichino, A.-M., Carsillo, T., Carlson, A.L., Sari-Sarraf, F., Ramsauer, K.,
618 Debasitis, J.C., Maruggi, G., Otten, G.R., Geall, A.J., et al. (2017). Induction of an IFN-
619 Mediated Antiviral Response by a Self-Amplifying RNA Vaccine: Implications for Vaccine
620 Design. J. Immunol. *198*, 4012–4024. https://doi.org/10.4049/jimmunol.1601877.

621 31. Sollberger, G., Streeck, R., Apel, F., Caffrey, B.E., Skoultchi, A.I., and Zychlinsky, A. (2020).
622 Linker histone H1.2 and H1.4 affect the neutrophil lineage determination. eLife *9*, e52563.
623 https://doi.org/10.7554/eLife.52563.

624 32. Behrends, M., and Engmann, O. (2020). Linker histone H1.5 is an underestimated factor in
625 differentiation and carcinogenesis. Environ. Epigenetics *6*, dvaa013.
626 https://doi.org/10.1093/eep/dvaa013.

627 33. Hornung, V., Hartmann, R., Ablasser, A., and Hopfner, K.-P. (2014). OAS proteins and
628 cGAS: unifying concepts in sensing and responding to cytosolic nucleic acids. Nat. Rev.
629 Immunol. *14*, 521–528. https://doi.org/10.1038/nri3719.

630 34. Wu, Y.-Y., Xing, J., Li, X.-F., Yang, Y.-L., Shao, H., and Li, J. (2023). Roles of interferon
631 induced protein with tetratricopeptide repeats (IFIT) family in autoimmune disease.
632 Autoimmun. Rev. *22*, 103453. https://doi.org/10.1016/j.autrev.2023.103453.

633 35. Betancor, G. (2023). You Shall Not Pass: MX2 Proteins Are Versatile Viral Inhibitors.
634 Vaccines *11*, 930. https://doi.org/10.3390/vaccines11050930.

635 36. Jimenez, F., Quinones, M.P., Martinez, H.G., Estrada, C.A., Clark, K., Garavito, E., Ibarra,
636 J., Melby, P.C., and Ahuja, S.S. (2010). CCR2 Plays a Critical Role in Dendritic Cell
637 Maturation: Possible Role of CCL2 and NF-κB. J. Immunol. *184*, 5571–5581.
638 https://doi.org/10.4049/jimmunol.0803494.

639 37. Peters, W., Scott, H.M., Chambers, H.F., Flynn, J.L., Charo, I.F., and Ernst, J.D. (2001).
640 Chemokine receptor 2 serves an early and essential role in resistance to Mycobacterium
641 tuberculosis. Proc. Natl. Acad. Sci. *98*, 7958–7963.
642 https://doi.org/10.1073/pnas.131207398.

643 38. Granucci, F., Vizzardelli, C., Pavelka, N., Feau, S., Persico, M., Virzi, E., Rescigno, M.,
644 Moro, G., and Ricciardi-Castagnoli, P. (2001). Inducible IL-2 production by dendritic cells
645 revealed by global gene expression analysis. Nat. Immunol. *2*, 882–888.
646 https://doi.org/10.1038/ni0901-882.

647 39. Celis-Gutierrez, J., Blattmann, P., Zhai, Y., Jarmuzynski, N., Ruminski, K., Grégoire, C.,
648 Ounoughene, Y., Fiore, F., Aebersold, R., Roncagalli, R., et al. (2019). Quantitative
649 Interactomics in Primary T Cells Provides a Rationale for Concomitant PD-1 and BTLA

650 Coinhibitor Blockade in Cancer Immunotherapy. Cell Rep. *27*, 3315-3330.e7.
651 https://doi.org/10.1016/j.celrep.2019.05.041.

652 40. Karikó, K., Buckstein, M., Ni, H., and Weissman, D. (2005). Suppression of RNA
653 Recognition by Toll-like Receptors: The Impact of Nucleoside Modification and the
654 Evolutionary Origin of RNA. Immunity *23*, 165–175.
655 https://doi.org/10.1016/j.immuni.2005.06.008.

656 41. Lin, J., Harding, A., Giurisato, E., and Shaw, A.S. (2009). KSR1 Modulates the Sensitivity of
657 Mitogen-Activated Protein Kinase Pathway Activation in T Cells without Altering
658 Fundamental System Outputs. Mol. Cell. Biol. *29*, 2082–2091.
659 https://doi.org/10.1128/MCB.01634-08.

660 42. Goettel, J.A., Algood, H.M.S., Olivares–Villagómez, D., Washington, M.K., Chaturvedi, R.,
661 Wilson, K.T., Kaer, L.V., and Polk, D.B. (2011). KSR1 Protects From Interleukin-10
662 Deficiency-Induced Colitis in Mice by Suppressing T-Lymphocyte Interferon-γ Production.
663 Gastroenterology *140*, 265–274. https://doi.org/10.1053/j.gastro.2010.09.041.

664 43. Duong, V.-T., Lee, D., Kim, Y.H., and Oh, S.-O. (2024). Functional role of UNC13D in
665 immune diseases and its therapeutic applications. Front. Immunol. *15*.
666 https://doi.org/10.3389/fimmu.2024.1460882.

667 44. Wu, D., Xiang, L., Peng, L., Gu, H., Tang, Y., Luo, H., Liu, H., and Wang, Y. (2022).
668 Comprehensive analysis of the immune implication of FABP4 in colon adenocarcinoma.
669 PLOS ONE *17*, e0276430. https://doi.org/10.1371/journal.pone.0276430.

670 45. Lenart, K., Hellgren, F., Ols, S., Yan, X., Cagigi, A., Cerveira, R.A., Winge, I., Hanczak, J.,
671 Mueller, S.O., Jasny, E., et al. (2022). A third dose of the unmodified COVID-19 mRNA
672 vaccine CVnCoV enhances quality and quantity of immune responses. Mol. Ther. - Methods
673 Clin. Dev. *27*, 309–323. https://doi.org/10.1016/j.omtm.2022.10.001.

674 46. Anderluzzi, G., Lou, G., Gallorini, S., Brazzoli, M., Johnson, R., O'Hagan, D.T., Baudner,
675 B.C., and Perrie, Y. (2020). Investigating the Impact of Delivery System Design on the
676 Efficacy of Self-Amplifying RNA Vaccines. Vaccines *8*, 212.
677 https://doi.org/10.3390/vaccines8020212.

678 47. Anderluzzi, G., Lou, G., Woods, S., Schmidt, S.T., Gallorini, S., Brazzoli, M., Johnson, R.,
679 Roberts, C.W., O'Hagan, D.T., Baudner, B.C., et al. (2022). The role of nanoparticle format
680 and route of administration on self-amplifying mRNA vaccine potency. J. Controlled Release
681 *342*, 388–399. https://doi.org/10.1016/j.jconrel.2021.12.008.

682 48. Choi, Y.S., Eto, D., Yang, J.A., Lao, C., and Crotty, S. (2013). Cutting Edge: STAT1 Is
683 Required for IL-6–Mediated Bcl6 Induction for Early Follicular Helper Cell Differentiation. J.
684 Immunol. *190*, 3049–3053. https://doi.org/10.4049/jimmunol.1203032.

685 49. Zhou, P., Liang, K., and Yu, D. (2019). Germinal center TFH cells: T(w)o be or not t(w)o be,
686 IL-6 is the answer. Sci. Immunol. *4*, eaay7668. https://doi.org/10.1126/sciimmunol.aay7668.

687 50. Papillion, A., Powell, M.D., Chisolm, D.A., Bachus, H., Fuller, M.J., Weinmann, A.S.,
688 Villarino, A., O'Shea, J.J., León, B., Oestreich, K.J., et al. (2019). Inhibition of IL-2

689 responsiveness by IL-6 is required for the generation of GC-TFH cells. Sci. Immunol. *4*,
690 eaaw7636. https://doi.org/10.1126/sciimmunol.aaw7636.

691 51. Liang, F., Lindgren, G., Lin, A., Thompson, E.A., Ols, S., Röhss, J., John, S., Hassett, K.,
692 Yuzhakov, O., Bahl, K., et al. (2017). Efficient Targeting and Activation of Antigen-
693 Presenting Cells In Vivo after Modified mRNA Vaccine Administration in Rhesus Macaques.
694 Mol. Ther. *25*, 2635–2647. https://doi.org/10.1016/j.ymthe.2017.08.006.

695 52. Maruggi, G., Mallett, C.P., Westerbeck, J.W., Chen, T., Lofano, G., Friedrich, K., Qu, L.,
696 Sun, J.T., McAuliffe, J., Kanitkar, A., et al. (2022). A self-amplifying mRNA SARS-CoV-2
697 vaccine candidate induces safe and robust protective immunity in preclinical models. Mol.
698 Ther. *30*, 1897–1912. https://doi.org/10.1016/j.ymthe.2022.01.001.

699 53. Lazzaro, S., Giovani, C., Mangiavacchi, S., Magini, D., Maione, D., Baudner, B., Geall, A.J.,
700 De Gregorio, E., D'Oro, U., and Buonsanti, C. (2015). CD8 T-cell priming upon mRNA
701 vaccination is restricted to bone-marrow-derived antigen-presenting cells and may involve
702 antigen transfer from myocytes. Immunology *146*, 312–326.
703 https://doi.org/10.1111/imm.12505.

704 54. Kranz, L.M., Diken, M., Haas, H., Kreiter, S., Loquai, C., Reuter, K.C., Meng, M., Fritz, D.,
705 Vascotto, F., Hefesha, H., et al. (2016). Systemic RNA delivery to dendritic cells exploits
706 antiviral defence for cancer immunotherapy. Nature *534*, 396–401.
707 https://doi.org/10.1038/nature18300.

708 55. Fujisawa, M., Onodera, T., Kuroda, D., Kewcharoenwong, C., Sasaki, M., Itakura, Y.,
709 Yumoto, K., Nithichanon, A., Ito, N., Takeoka, S., et al. (2025). Molecular convergence of
710 neutralizing antibodies in human revealed by repeated rabies vaccination. Npj Vaccines *10*,
711 1–14. https://doi.org/10.1038/s41541-025-01073-5.

712 56. Callaway, H.M., Zyla, D., Larrous, F., de Melo, G.D., Hastie, K.M., Avalos, R.D., Agarwal,
713 A., Corti, D., Bourhy, H., and Saphire, E.O. Structure of the rabies virus glycoprotein trimer
714 bound to a prefusion-specific neutralizing antibody. Sci. Adv. *8*, eabp9151.
715 https://doi.org/10.1126/sciadv.abp9151.

716 57. de Alwis, R., Gan, E.S., Chen, S., Leong, Y.S., Tan, H.C., Zhang, S.L., Yau, C., Low,
717 J.G.H., Kalimuddin, S., Matsuda, D., et al. (2021). A single dose of self-transcribing and
718 replicating RNA-based SARS-CoV-2 vaccine produces protective adaptive immunity in
719 mice. Mol. Ther. *29*, 1970–1983. https://doi.org/10.1016/j.ymthe.2021.04.001.

720 58. Immunogenicity of BA.5 Bivalent mRNA Vaccine Boosters (2023). N Engl J Med.

721 59. Antibody Response to Omicron BA.4–BA.5 Bivalent Booster (2023). N Engl J Med.

722 60. Kim, S., Jeon, J.H., Kim, M., Lee, Y., Hwang, Y.-H., Park, M., Li, C.H., Lee, T., Lee, J.-A.,
723 Kim, Y.-M., et al. (2024). Innate immune responses against mRNA vaccine promote cellular
724 immunity through IFN-β at the injection site. Nat. Commun. *15*, 7226.
725 https://doi.org/10.1038/s41467-024-51411-9.

726 61. Fleischmann, E., Middelkamp, V., and van den Broek, T. (2025). Deciphering the Human
727 Germinal Center: A Review of Models to Study T–B Cell Interactions. Eur. J. Immunol. *55*,
728 e202451460. https://doi.org/10.1002/eji.202451460.

62. Geall, A.J., Verma, A., Otten, G.R., Shaw, C.A., Hekele, A., Banerjee, K., Cu, Y., Beard, C.W., Brito, L.A., Krucker, T., et al. (2012). Nonviral delivery of self-amplifying RNA vaccines. Proc. Natl. Acad. Sci. *109*, 14604–14609. https://doi.org/10.1073/pnas.1209367109.

63. Jeffs, L.B., Palmer, L.R., Ambegia, E.G., Giesbrecht, C., Ewanick, S., and MacLachlan, I. (2005). A Scalable, Extrusion-Free Method for Efficient Liposomal Encapsulation of Plasmid DNA. Pharm. Res. *22*, 362–372. https://doi.org/10.1007/s11095-004-1873-z.

64. Lou, G., Anderluzzi, G., Schmidt, S.T., Woods, S., Gallorini, S., Brazzoli, M., Giusti, F., Ferlenghi, I., Johnson, R.N., Roberts, C.W., et al. (2020). Delivery of self-amplifying mRNA vaccines by cationic lipid nanoparticles: The impact of cationic lipid selection. J. Controlled Release *325*, 370–379. https://doi.org/10.1016/j.jconrel.2020.06.027.

65. Li, J., Van Vranken, J.G., Pontano Vaites, L., Schweppe, D.K., Huttlin, E.L., Etienne, C., Nandhikonda, P., Viner, R., Robitaille, A.M., Thompson, A.H., et al. (2020). TMTpro reagents: a set of isobaric labeling mass tags enables simultaneous proteome-wide measurements across 16 samples. Nat. Methods *17*, 399–404. https://doi.org/10.1038/s41592-020-0781-4.

66. Eng, J.K., Jahan, T.A., and Hoopmann, M.R. (2013). Comet: An open-source MS/MS sequence database search tool. PROTEOMICS *13*, 22–24. https://doi.org/10.1002/pmic.201200439.

67. Elias, J.E., and Gygi, S.P. (2007). Target-decoy search strategy for increased confidence in large-scale protein identifications by mass spectrometry. Nat. Methods *4*, 207–214. https://doi.org/10.1038/nmeth1019.

68. Xu, S., Hu, E., Cai, Y., Xie, Z., Luo, X., Zhan, L., Tang, W., Wang, Q., Liu, B., Wang, R., et al. (2024). Using clusterProfiler to characterize multiomics data. Nat. Protoc., 1–29. https://doi.org/10.1038/s41596-024-01020-z.

69. Thompson, J.D., Higgins, D.G., and Gibson, T.J. (1994). CLUSTAL W: improving the sensitivity of progressive multiple sequence alignment through sequence weighting, position-specific gap penalties and weight matrix choice. Nucleic Acids Res. *22*, 4673–4680. https://doi.org/10.1093/nar/22.22.4673.

70. Letunic, I., and Bork, P. (2021). Interactive Tree Of Life (iTOL) v5: an online tool for phylogenetic tree display and annotation. Nucleic Acids Res. *49*, W293–W296. https://doi.org/10.1093/nar/gkab301.

763 **FIGURES**

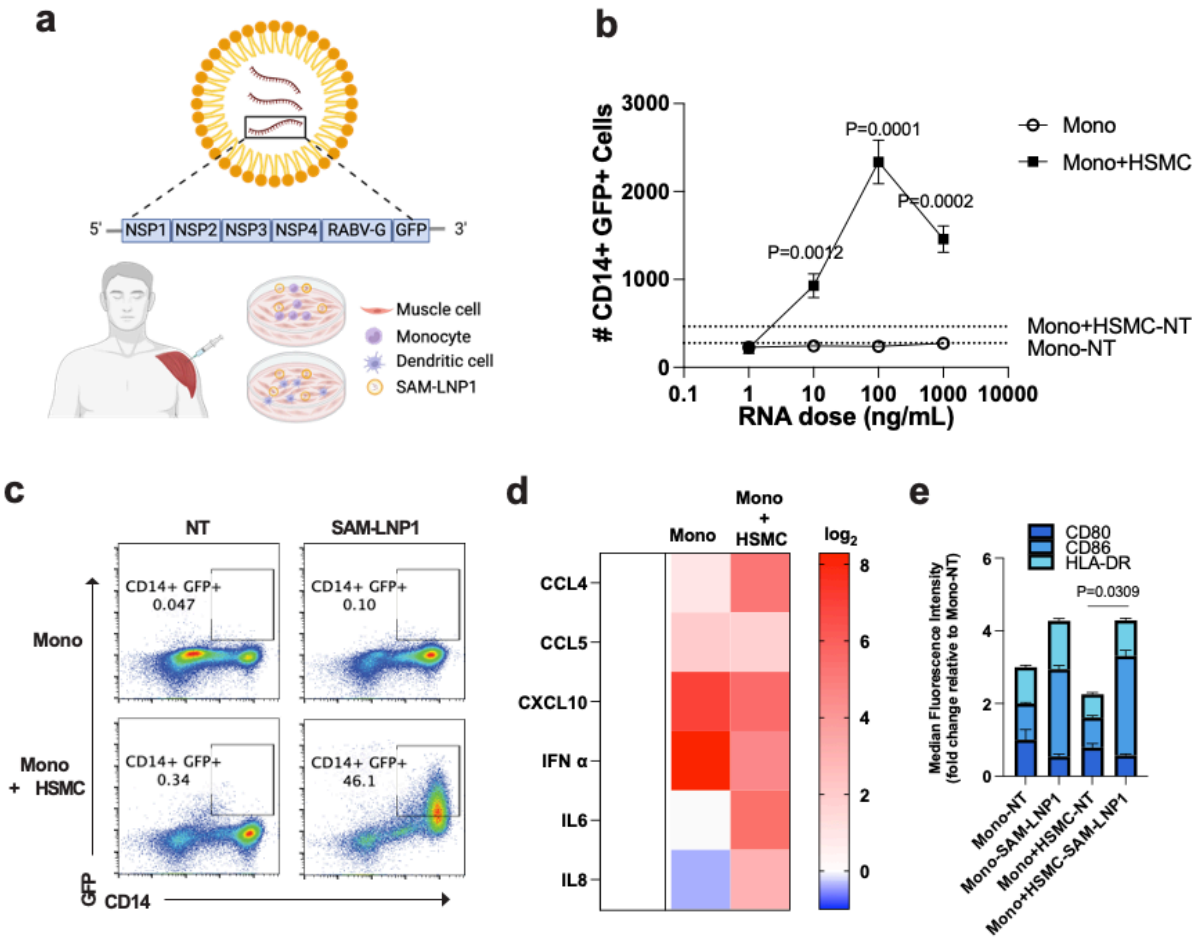

764

765 **Fig. 1. *In vitro* model of intramuscular vaccination using SAM-LNP. a,** Schematic of the
766 intramuscular vaccination model. **b,** Quantification of live CD14^{+} GFP cells by flow cytometry in
767 monocyte (Mono) monoculture and in co-culture with HSMC (Mono+HSMC) without treatment
768 ("no treatment", NT) or various doses of SAM-LNP1. **c,** Density dot plots illustrating GFP
769 expression in NT and 100ng/ml SAM-LNP1treated groups. **d,** Cytokine levels detected using a
770 Meso Scale Discovery assay, comparing NT and 100 ng/ml SAM-LNP1in Mono and Mono+HSMC
771 conditions. Fold change (log2) in SAM-LNP1 treated cultures relative to NT cultures is displayed.
772 **e,** Detection of myeloid activation markers CD80, CD86, and HLA-DR by flow cytometry,
773 comparing NT and 100 ng/ml SAM-LNP1in both Mono and Mono+HSMC settings. Representative
774 results from one donor are shown, with similar outcomes observed in at least three donors. In **b**

775 and **e**, mean values from 3 wells are shown. Error bars indicate standard deviation (SD). An
776 unpaired t-test was performed in panel **b**, and two-way ANOVA in panel **e**.

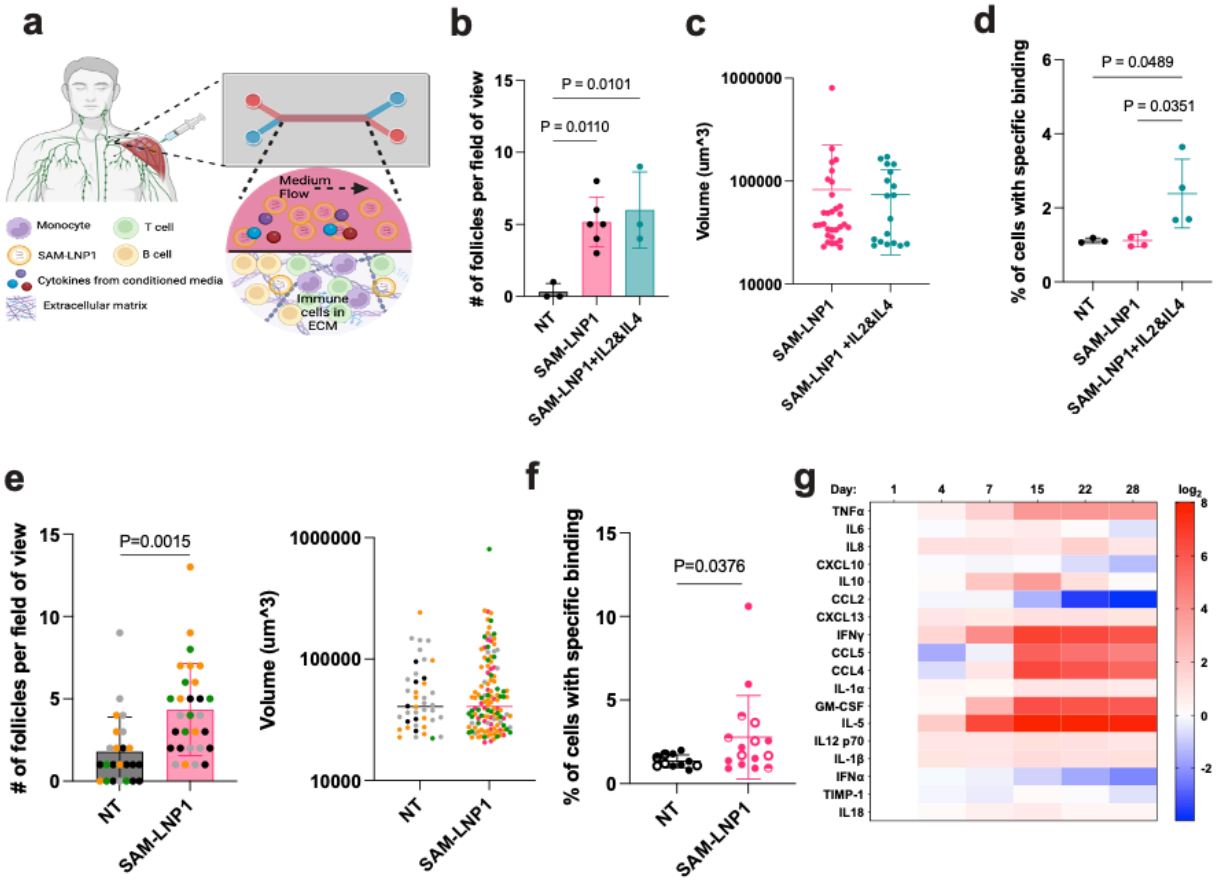

777

778 **Fig. 2. Induction of LFs and anti-RABV-G IgG production by SAM-LNP1 in human LF Chips.**
779 **a,** Schematic of the LF chip created with monocytes and conditioned medium from intramuscular
780 vaccination mimicking module. Quantification of the number (**b**) and size (**c**) of LFs in LF chips of
781 one donor based on immunostaining followed by confocal imaging. Each data point represents
782 one field of view (**b**) or an individual follicle (**c**). **d,** Anti-RABV-G IgG levels in effluents of no
783 treatment LF chips or chips vaccinated with or without IL2 and IL4 and cultured for 14 days were
784 detected using a cell-based assay. **e,** Quantification of the number (left) and size (right) of LFs in
785 LF chips from four different donors, with each color representing a different donor. Each data
786 point corresponds to one field of view (left) or an individual follicle (right). **f,** Anti-RABV-G IgG
787 levels in effluents of LF chips. Each data point represents one chip, with different symbols

788 indicating chips from three independent donors. **g,** Heatmap showing Log2 fold changes in
789 cytokine levels in LF chip effluents, measured using a Luminex® Multiplex Assay at various time
790 points (4, 7, 15, 22, and 28 days post-vaccination) compared to day 1. Data shown are mean ±
791 SD; **b, c, d** and **e**, One way ANOVA test, **f**, unpaired t-test.

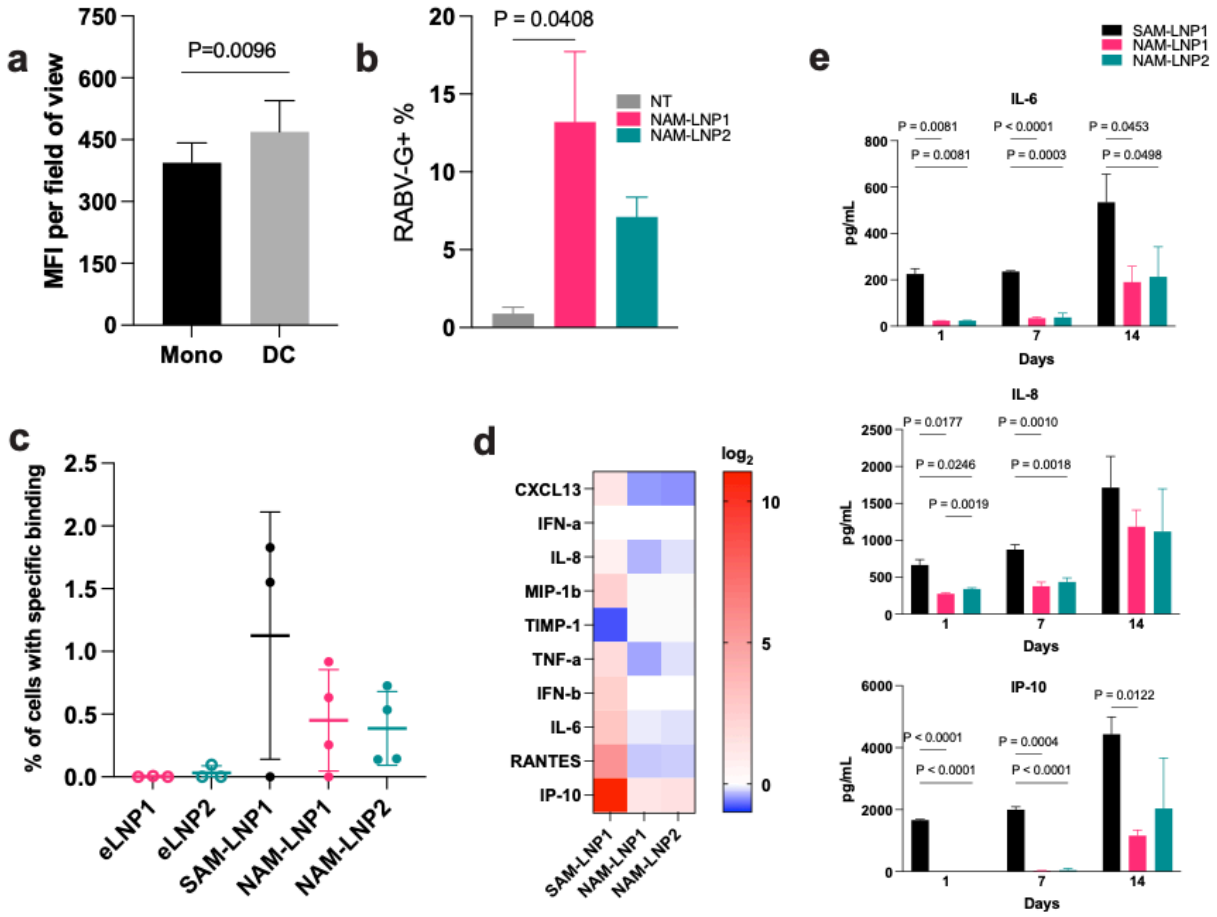

792

793 **Fig. 3. Induction of anti-RABV-G IgG and cytokine release by non-replicating mRNA. a,**
794 Quantification of monocytes and DCs after a one-day co-culture with HSMC and 1000 ng/mL of
795 NAM-LNP1, assessed using immunofluorescence staining and detected by high-throughput
796 imaging. Each data point represents the median fluorescence intensity (MFI) from a single field
797 of view. **b,** Quantification of RABV-G^{+} DCs, by flow cytometry, one day after exposure to either
798 1000 ng/mL of NAM-LNP1 or NAM-LNP2. **c,** Anti-RABV-G IgG levels were detected in the
799 effluents of LF chips cultured for 14 days using a cell-based assay. Each vaccine was tested in 2

donors, and similar results were obtained. **d,** Heatmap showing Log2 fold changes in cytokine levels measured via a Meso Scale Discovery assay in supernatants from HSMC-DC coculture, one day after treatment with SAM-LNP1, NAM-LNP1, and NAM-LNP2 as compared to the empty LNP control. **e,** Fold change in IL-6, IL-8, and IP-10 levels measured via a Meso Scale Discovery assay in supernatants from LF chips, 1, 7, and 14 days after treatment with SAM-LNP1, NAM-LNP1, and NAM-LNP2 as compared to the empty LNP control. Data points represent individual chips. Data shown are mean ± SD; **a,** unpaired t-test; **b** and **c**, one-way ANOVA test; **e**, two-way ANOVA test.

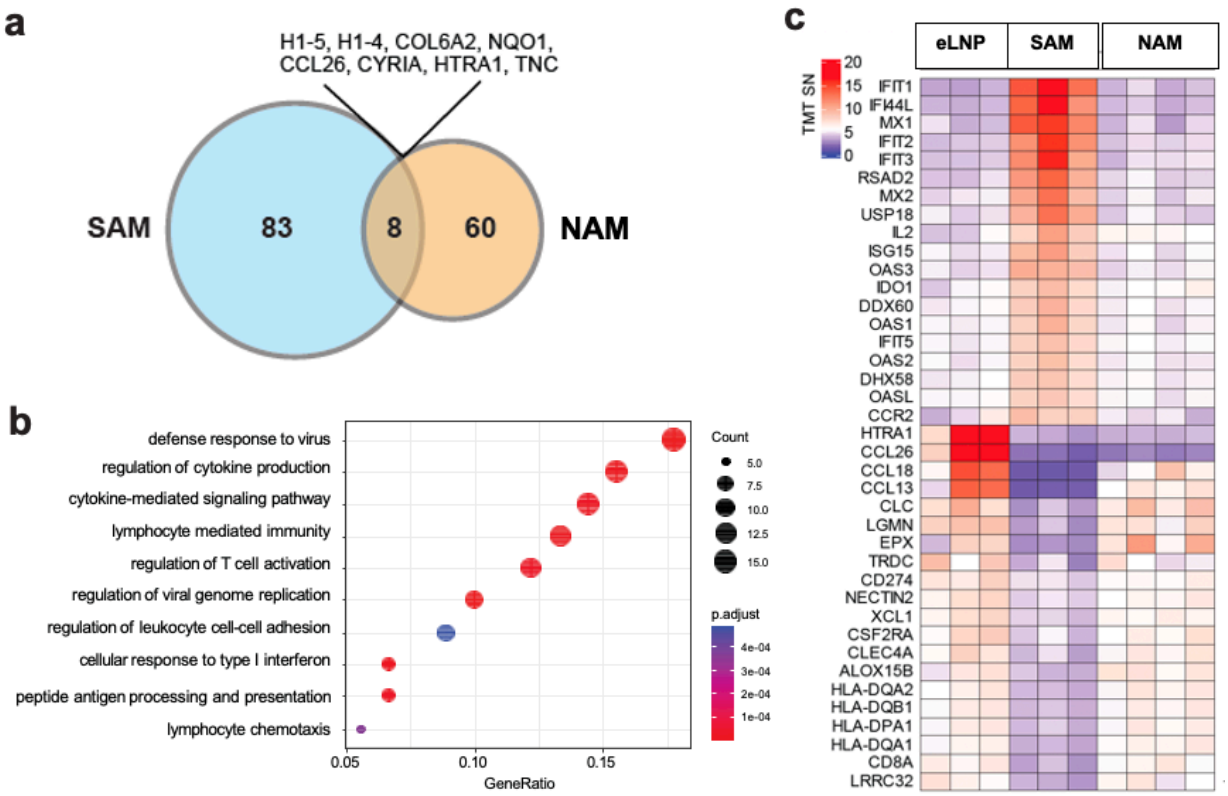

Fig. 4. Different proteomic responses induced by self-amplifying mRNA and non-amplifying mRNA vaccines. a, Venn diagram showing the number of overlapping vs. distinct protein perturbations induced by SAM-LNP1 and NAM-LNP1. **b,** Gene ontology analysis highlights biological processes predominantly regulated by SAM-LNP1 compared to the empty

LNP1. **c,** Heatmap illustrating the top differentially expressed proteins, labeled by gene locus name, showcasing the extent of regulation by the treatments.

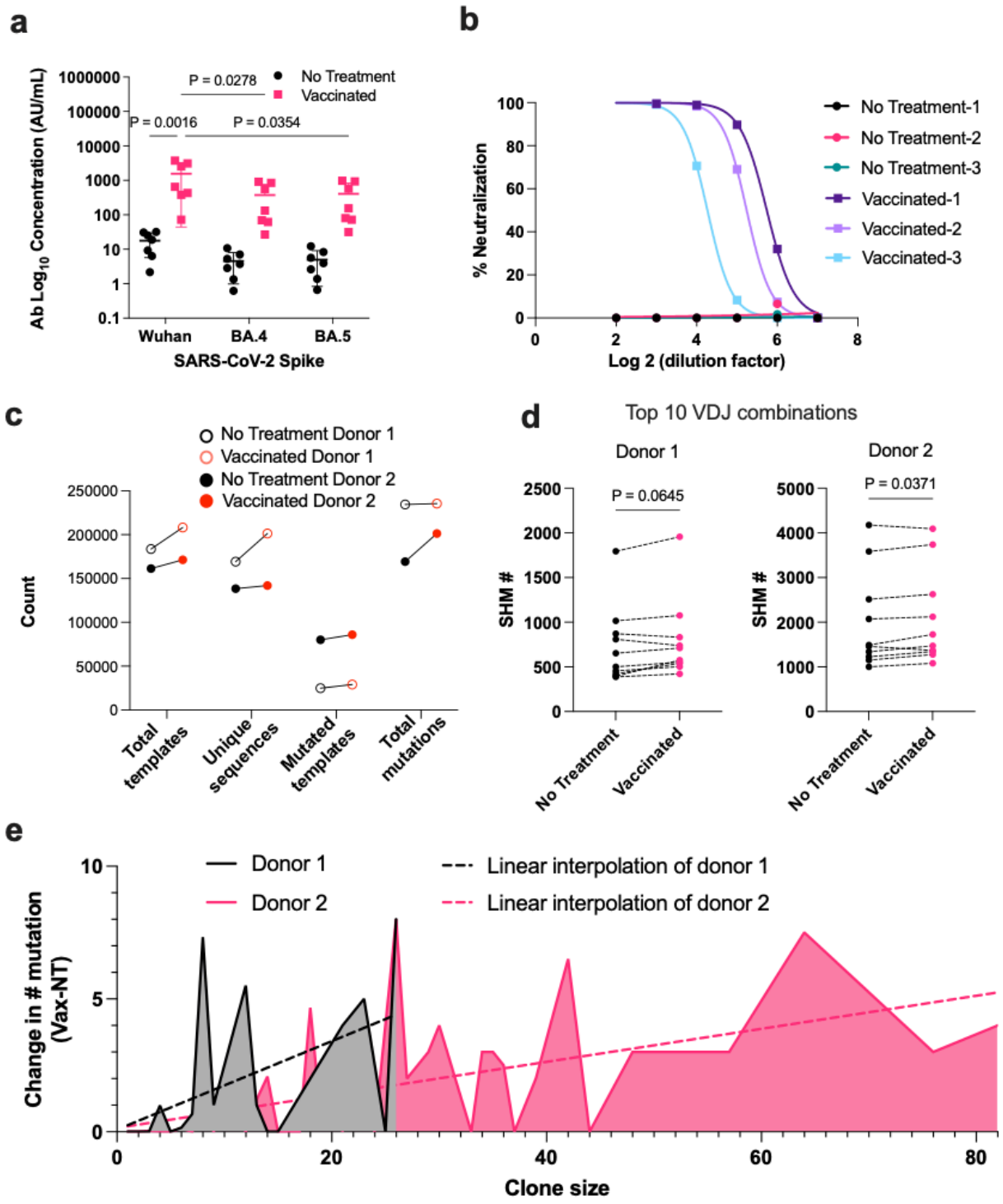

816 **Fig. 5. Induction of spike-specific neutralizing antibodies and somatic hypermutation in LF**
817 **chips following vaccination with Moderna bivalent COVID-19 vaccine. a,** Moderna bivalent
818 COVID-19 vaccine was administered at 500 ng/ml (M500). Day 9 LF chip outflows post-
819 vaccination (M500) and no treatment (NT) were tested to determine COVID-19 spike-specific IgG
820 concentrations using the Meso Scale Discovery (MSD) V-PLEX SARS-CoV-2 Panel 27 (IgG) Kit.
821 **b,** Neutralization by outflows from each no treatment or vaccinated chip created from the cells of
822 one individual donor is depicted. 0% neutralization is defined by the luciferase signal in cells
823 infected with SARS-CoV-2 pseudovirus using fresh medium controls, and 100% neutralization
824 corresponds to the signal in uninfected cells. Similar results were obtained from a 2nd donor's cells.
825 **c,** BCR repertoire analysis on LF chips from two donors. Total templates, unique sequences,
826 mutated templates, and total mutations of DNA templates from cells recovered from both
827 vaccinated (M500) and no treatment chips from two donors are shown. **d,** Comparison of SHM
828 counts of top 10 V-D-J combinations from both vaccinated (M500) and no treatment chips from
829 both donors. **e,** Changes in average SHM in vaccinated samples compared to unvaccinated
830 samples across both donors. Data shown are mean ± SD, **a,** two-way ANOVA test, **d,** Wilcoxon
831 matched pairs signed rank test.

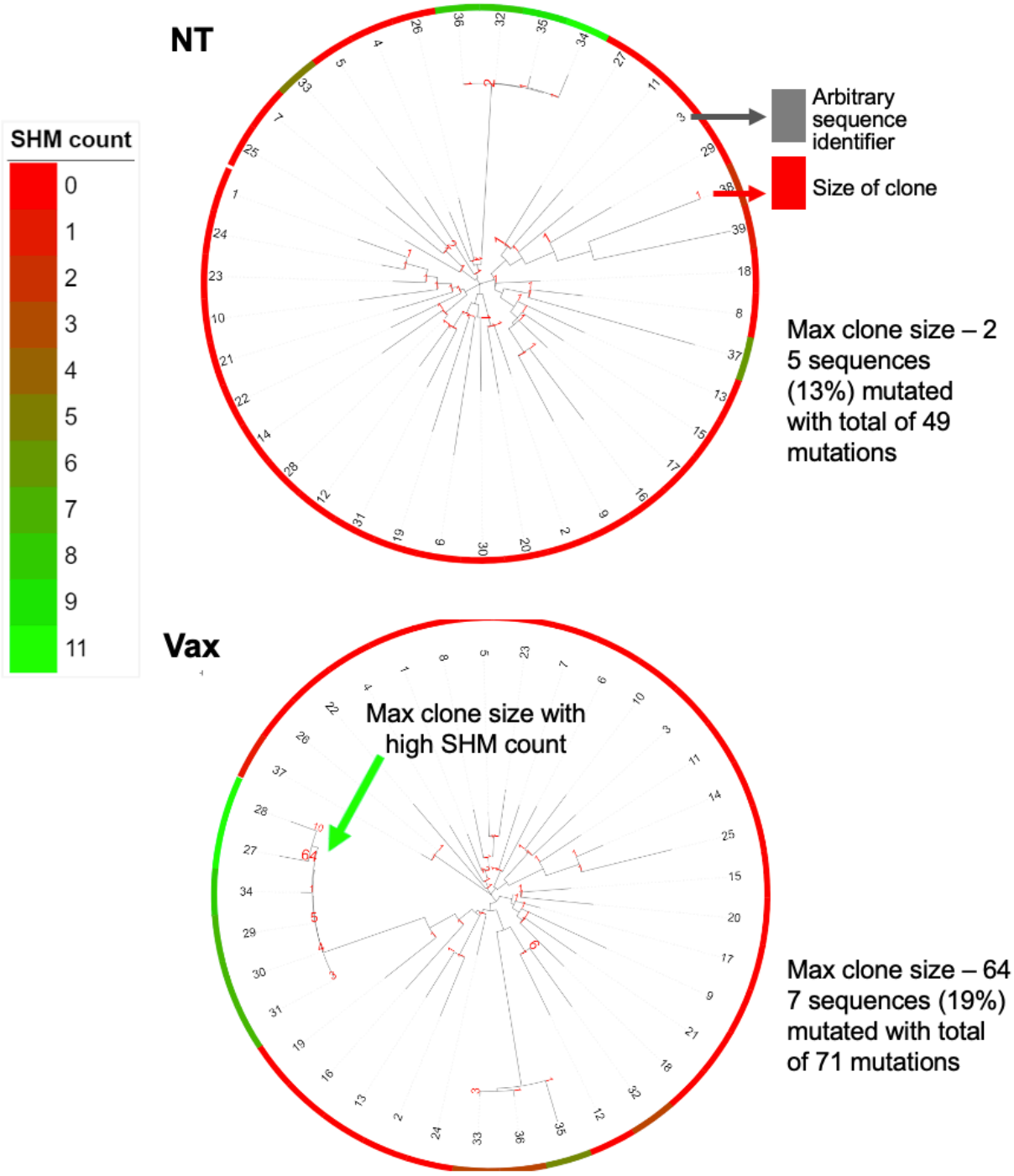

Fig. 6. Clonal Expansion and Somatic Hypermutation in LF Chips.

Clonal sequences of BCR containing the V-D-J genes IGHV01-69, IGHD04-23*01, and IGHJ06-01*02 were analyzed using ClustalW for alignment. Phylogenetic analysis was subsequently visualized with iTol, generating the depicted dendrograms. **a,** Dendrogram of sequences from no

837 treatment chips. **b,** Dendrogram of sequences from chips vaccinated with 500ng/ml Moderna
838 bivalent COVID-19 vaccine. Colors on the outer ring indicate the number of mutations per
839 sequence. Branch labels represent the size of each clone, and the numbers within the ring serve
840 as arbitrary sequence identifiers.

841

842 **SUPPLEMENTARY FIGURES**

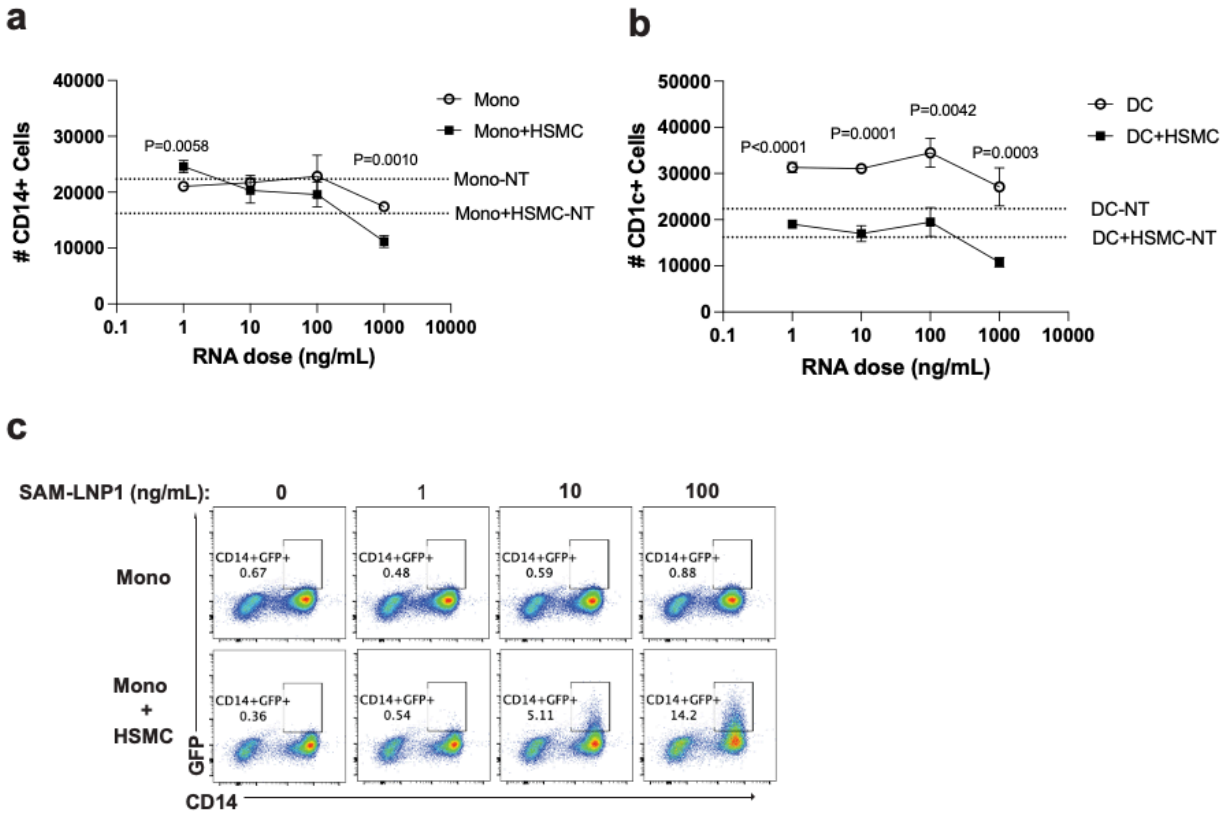

843

844 **Supplementary Fig. 1. Dose-dependent effects of SAM-LNP1 on antigen-presenting cells**
845 **(APCs) and human skeletal muscle cells (HSMCs).** Quantification of **a,** live $CD14^+$ monocytes.
846 **b,** live $CD1c^+$ DCs in monoculture and co-culture under no treatment (NT) or various doses of
847 SAM-LNP, measured by flow cytometry. **c,** Monocyte uptake of SAM-LNP1 in co-culture with
848 HSMCs, showing a dose-dependent pattern represented through percentage changes in flow
849 cytometry data. Representative results from one donor, with similar results obtained in at least

850 three donors. Data shown are mean values from 3 wells ± SD; an unpaired t-test was performed

851 for **a** and **b.**

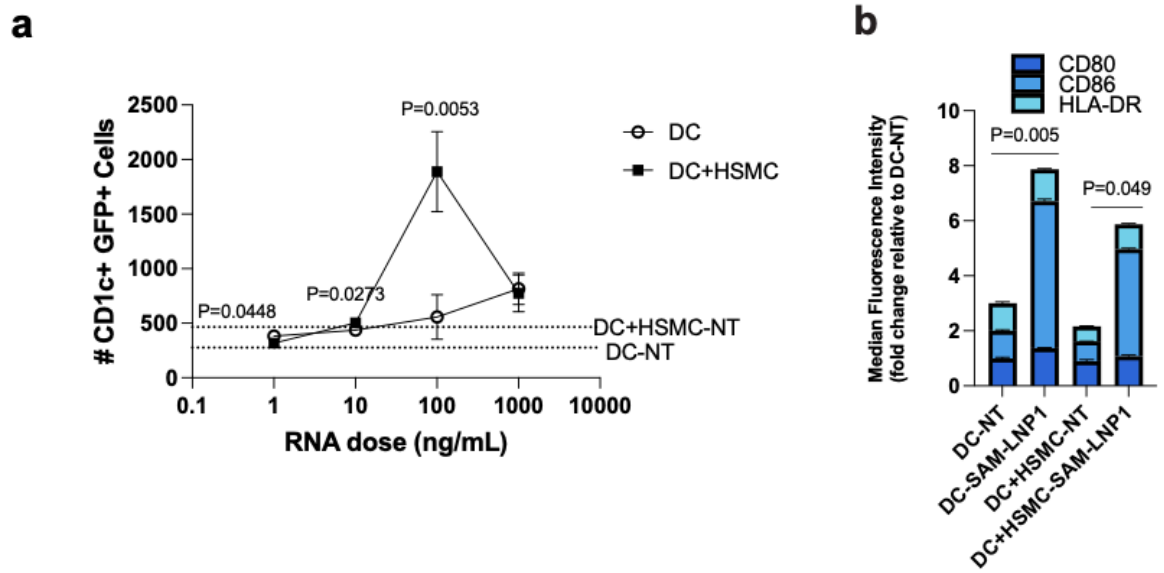

852

853 **Supplementary Fig. 2. Dose-dependent effects of SAM-LNP1 on DCs and HSMCs.**

854 **a,** Quantification of live CD1c^{+} GFP^{+} DCs recovered from monocultures (DC) or co-cultures with

855 human skeletal muscle cells (DC+HSMC) under no treatment (NT) or various doses of SAM-

856 LNP1, using flow cytometry. **b,** Detection of DC activation markers CD80, CD86, and HLA-DR by

857 flow cytometry, comparing NT to 100 ng/ml SAM-LNP1 in DC alone (DC) and DC-muscle cell co-

858 culture (DC+HSMC) conditions. Representative results from one donor, with similar results

859 obtained in at least three donors. Data shown are mean values from 3 wells ± SD; an unpaired t-

860 test was performed for **a**.

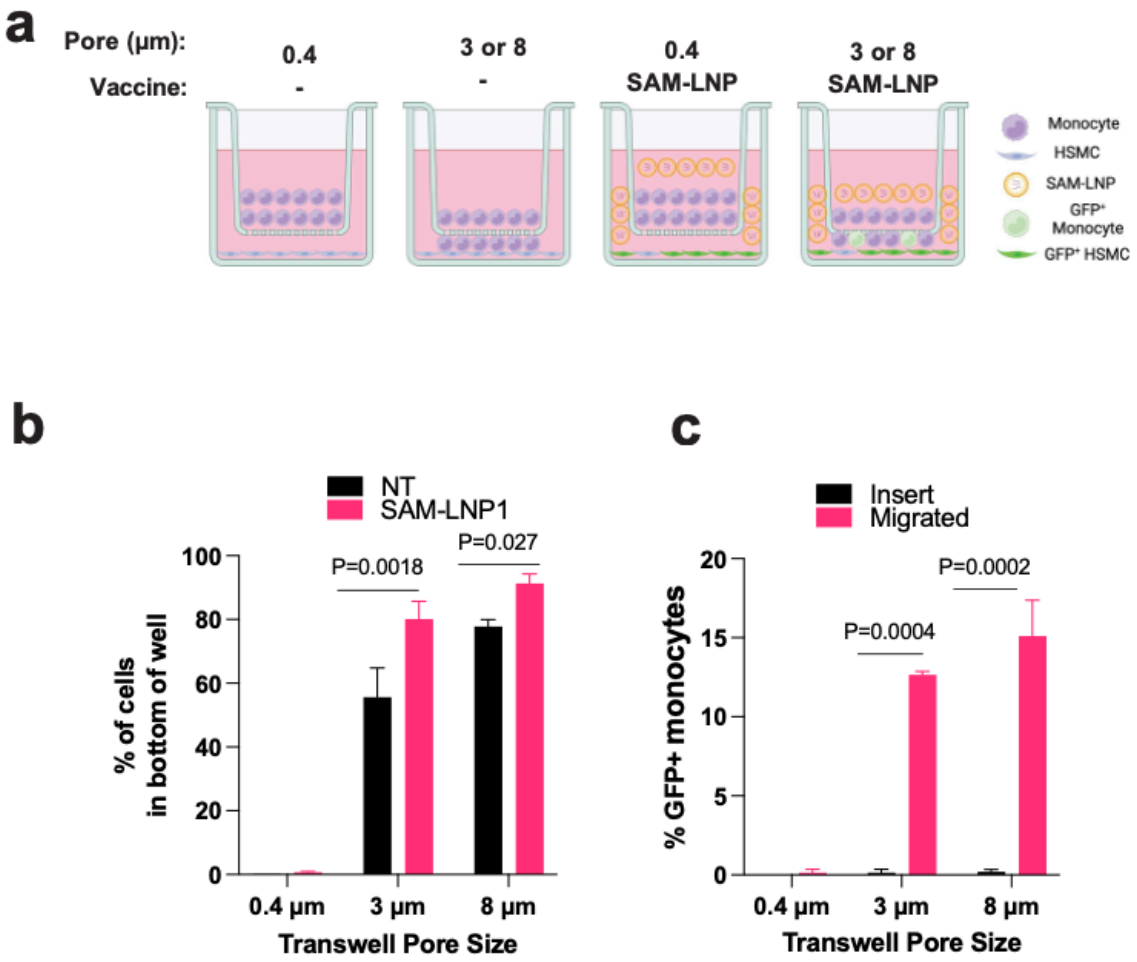

Supplementary Fig. 3. Requirement of direct cell-cell contact for antigen expression induced by SAM-LNP1. a, Schematic of the TW experiment designed to test antigen uptake by monocytes and HSMC. **b,** Total monocytes recovered from both the insert and the bottom of TWs with 0.4 μm, 3 μm, and 8 μm pore sizes with no treatment (NT) or 100 ng/ml SAM-LNP1, collected separately and quantified via flow cytometry. **c,** Percentage of GFP+ monocytes in the insert or those that migrated to the HSMC monolayer in the bottom wells relative to the total number of monocytes collected from each location. Results from one donor are shown; similar outcomes were achieved in two additional experiments using monocytes from two different donors. Data shown are mean ± SD; n = 2 replicates in each group in **b** and **c**, unpaired t-test.

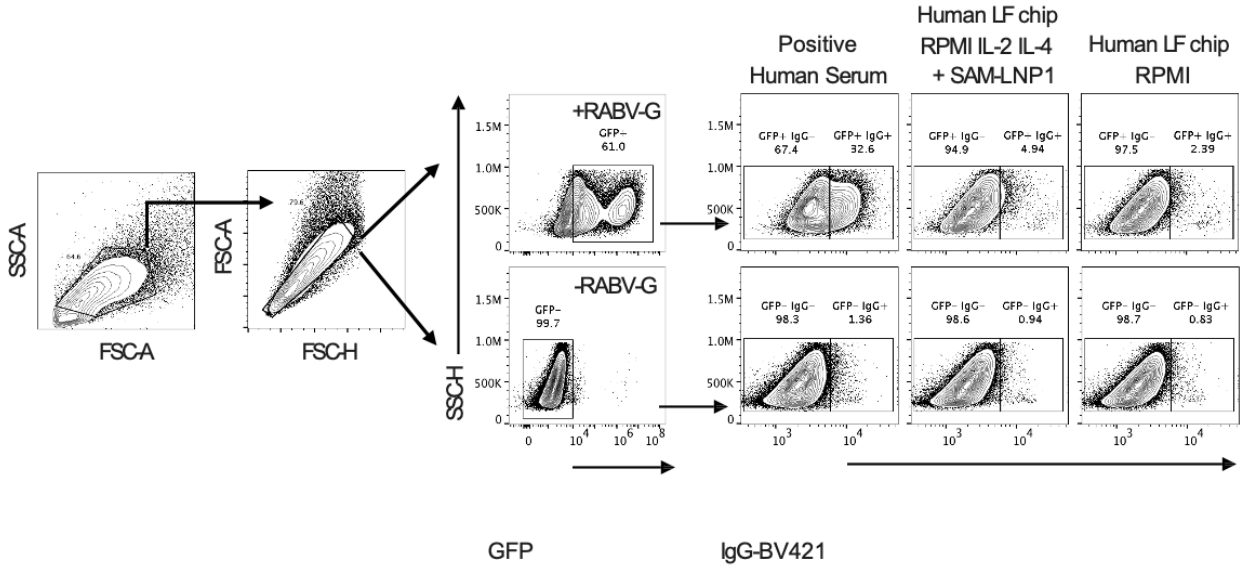

$$\text{\% of cells with specific binding: } 100 \times \frac{(\text{\% binding in +RABV-G cells} - \text{\% binding in –RABV-G cells})}{(100 - \text{\% binding in –RABV-G cells})}$$

Supplementary Fig. 4. Detection and quantification of anti-RABV-G IgG using a cell-based assay. Gating strategy used for quantifying anti-RABV-G IgG, including the formula employed to determine IgG levels.

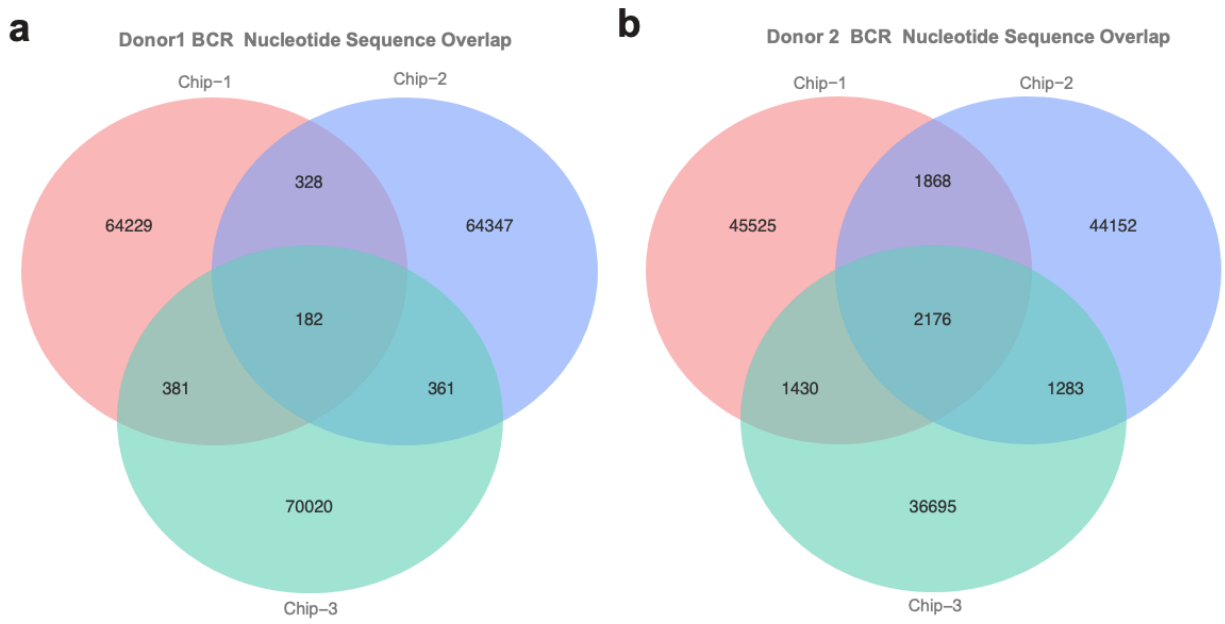

Supplementary Fig. 5. Overlap of BCR nucleotide sequences in vaccinated LF chips across two donors. Analysis of BCR sequence commonality in LF chips from individual donors following Moderna bivalent COVID-19 vaccine administration. **a,** BCR nucleotide sequence overlap in three LF chips from donor 1. **b,** BCR nucleotide sequence overlap in three LF chips from donor 2.

a

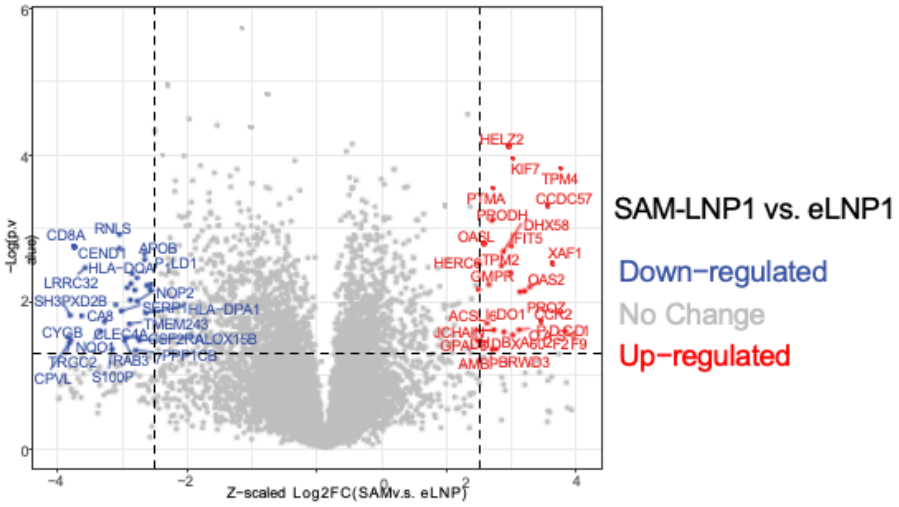
SAM-LNP1 vs. eLNP1
Down−regulated
No Change
Up−regulated
Z−scaled Log2FC(SAMv.s. eLNP)
−Log(p.value)

b

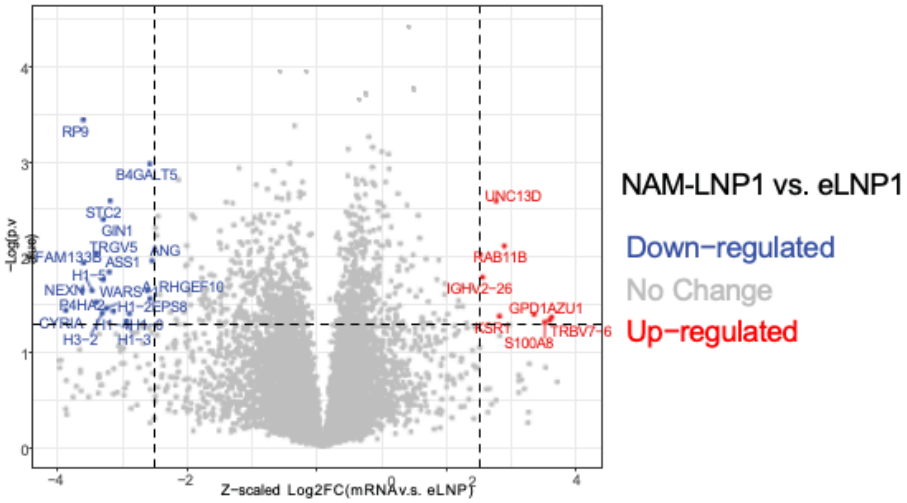
NAM-LNP1 vs. eLNP1
Down−regulated
No Change
Up−regulated
Z−scaled Log2FC(mRNAv.s. eLNP)
−Log(p.value)

c

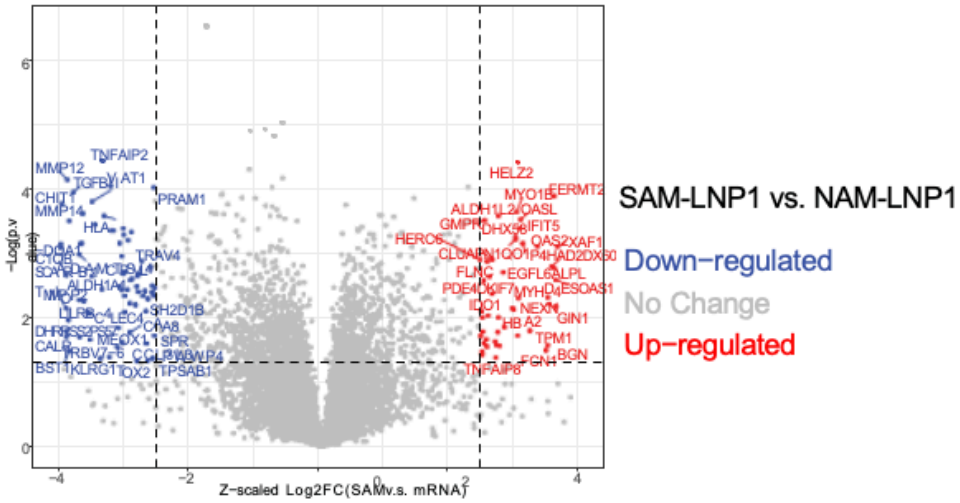
SAM-LNP1 vs. NAM-LNP1
Down−regulated
No Change
Up−regulated
Z−scaled Log2FC(SAMv.s. mRNA)
−Log(p.value)

885 **Supplementary Fig. 6. Comparative analysis of proteasome changes in vaccinated chips.**
886 Differential protein expression was assessed in LF chips following vaccination and visualized
887 through volcano plots. **a,** Volcano plot illustrating protein changes in cells from chips vaccinated
888 with SAM-LNP1 versus those treated with control empty LNP. **b,** Volcano plot showing protein
889 expression in cells from chips vaccinated with NAM-LNP1 compared to control empty LNP treated
890 chips. **c,** Volcano plot comparing protein expression in cells from SAM-LNP1 vaccinated chips to
891 those vaccinated with NAM-LNP1. P-values were adjusted for multiple comparisons using the
892 Bonferroni correction.
893